



Terahertz quasi-optical devices fabricated by 3D printing



Doctorado en ciencias (Óptica)

Advisor: Dr. Enrique Castro Camus

Student: Arturo Ignacio Hernandez Serrano

March 2018
León, Guanajuato, México

Abstract

In this thesis we theoretically and experimentally demonstrate four novel devices working at the THz range. We present the first 3D printed GRIN lens. Our measurements demonstrate how these lenses operate within the diffraction limit no matter what the polarization is, at least for the frequencies below 800 GHz ($\lambda > 375\mu m$). We also investigate the chromatic aberration. This new kind of lens shows some advantages compared with the conventional spherical lenses, given that they are thin and flat on both faces and their focal distances can be tailored by controlling the refractive-index gradient. In chapter 4 We experimentally demonstrate a novel 3D printed quasi-wollaston prism. The prism uses the birefringence induced in a sub-wavelength layered plastic-air structure that produces refraction in different directions for different polarizations. The component was simulated using the finite-difference-time-domain method, fabricated by 3D printing and subsequently tested by terahertz time-domain spectroscopy showing a polarization separation around of 23° for frequencies below 400 GHz, exhibiting cross polarization power extinction ratios better than 1.6×10^{-3} at 200 GHz. Chapter 5 is dedicated to the examination of, as the best of our knowledge, the first 3D printed q-plate with continuous birefringence variation for the generation of cylindrical vector beams at terahertz frequencies. This device can be used to efficiently couple terahertz radiation into waveguides, where they used segmented waveplates to generate radially polarized beams. Furthermore, other q-plates can be fabricated at low cost for the generation of complex-structured vector beams in order to study physical phenomena of interest in singular optics, such as angular momentum and polarization topologies. Finally in chapter 6 we demonstrate a stepped-refractive-index convergent lens made of a parallel stack of metallic plates for terahertz frequencies based on artificial dielectrics. The lens consist of a non-uniformly spaced stack of metallic plates, forming a mirror-symmetric array of parallel-plate waveguides (PPWGs). The operation of the device is based on the TE_1 mode of the PPWG. By varying the spacing between the plates, we can modify the local refractive index of the structure in every individual PPWG that constitutes the lens producing a stepped refractive index profile across the multi stack structure. These results show that this structure is capable of focusing a 1 cm diameter beam to a line focus of less than 4 mm for the design frequency of 0.18 THz. This structure shows that

this artificial-dielectric concept is an important technology for the fabrication of next generation terahertz devices.

List of Publications

- Hernandez-Serrano, A. I., Corzo-Garcia, S. C., Garcia-Sanchez, E., Alfaro, M., and Castro-Camus, E. (2014). Quality control of leather by terahertz time-domain spectroscopy. *Applied optics*, 53(33), 7872-7876.
- Hernandez-Serrano, A.I., Weidenbach, M., Busch, S.F., Koch, M. and Castro-Camus, E., 2016. Fabrication of gradient-refractive-index lenses for terahertz applications by three-dimensional printing. *JOSA B*, 33(5), pp.928-931.
- Corzo-Garcia, S.C., Hernandez-Serrano, A.I., Castro-Camus, E. and Mitrofanov, O., 2016. Monte Carlo simulation of near-field terahertz emission from semiconductors. *Physical Review B*, 94(4), p.045301.
- Gomez-Sepulveda, A.M., Hernandez-Serrano, A.I., Radpour, R., Koch-Dandolo, C.L., Rojas-Landeros, S.C., Ascencio-Rojas, L.F., Zarate, A., Hernandez, G., Gonzalez-Tirado, R.C., Insaurralde-Caballero, M. and Castro-Camus, E., 2017. History of Mexican Easel Paintings from an Altarpiece Revealed by Non-invasive Terahertz Time-Domain Imaging. *Journal of Infrared, Millimeter, and Terahertz Waves*, 38(4), pp.403-412.
- Hernandez-Serrano, A.I. and Castro-Camus, E., 2017. Quasi-Wollaston-Prism for Terahertz Frequencies Fabricated by 3D Printing. *Journal of Infrared, Millimeter, and Terahertz Waves*, 38(5), pp.567-573.
- Hernandez-Serrano, A.I., Castro-Camus, E. and Lopez-Mago, D., 2017. q-plate for the Generation of Terahertz Cylindrical Vector Beams Fabricated by 3D Printing. *Journal of Infrared, Millimeter, and Terahertz Waves*, pp.1-7.
- Dandolo, C.K., Gomez-Sepulveda, A.M., Hernandez-Serrano, A.I. and Castro-Camus, E., 2017. Examination of Painting on Metal Support by Terahertz Time-Domain Imaging. *Journal of Infrared, Millimeter, and Terahertz Waves*, 38(10), pp.1278-1287.
- Hernandez-Cardoso, G.G., Rojas-Landeros, S.C., Alfaro-Gomez, M., Hernandez-Serrano, A.I., Salas-Gutierrez, I., Lemus-Bedolla, E., Castillo-Guzman, A.R., Lopez-Lemus, H.L. and Castro-Camus, E., 2017. Terahertz imaging for early screening of diabetic foot syndrome: A proof of concept. *Scientific Reports*, 7.

- A. Hernandez-Serrano, Rajind Mendis, Kimberly S. Reichel, Wei Zhang, Enrique Castro-Camus, Daniel Mittleman, "Artificial dielectric stepped-refractive-index lens for the terahertz region." *Optics Express* (2018).

Acknowledgment

Firstly, I would like to express my gratitude to my advisor Dr. Enrique Castro Camus for the continuous support of my Ph.D study, for his patience and motivation. His guidance helped me in all the time of research and writing of this thesis. My sincere thanks also goes to CONACyT for the financial support (354621), without its support it would not be possible to conduct this research. Last but not the least, I would like to thank my family: my parents and to my sister for supporting me throughout writing this thesis.

Contents

1	Introduction	1
1.1	The terahertz gap	2
1.2	Terahertz time-domain-spectroscopy	4
1.2.1	THz-TDS setup	5
1.2.2	THz Emission/Detection using PCAs	8
1.2.3	Applications of Terahertz radiation	10
1.3	Objectives of this work	13
2	Three-dimensional printing	16
2.1	General steps of the 3D printing process	17
2.2	Terahertz applications of 3D printing	22
3	3D printed GRIN lens	23
3.1	Experimental setup	27
3.2	Results	29
3.2.1	Transverse measurements	29
3.2.2	Longitudinal measurements	29
4	3D printed polarization splitter	33
4.1	Device design and modeling	33
4.2	Experimental setup	37
4.3	Results	39
5	3D printed q-plate	42
5.1	Mathematical description	43
5.2	Fabrication and results	46
6	Artificial dielectric stepped-refractive-index lens	51
6.1	Design and Fabrication	52
6.2	Experimental characterization	55
7	Conclusion	61

Chapter 1

Introduction

Nowadays researches are turning their attention to the study of the light. This because many of the physical world phenomena involve electromagnetic radiation. Every living being is affected by both the amount of radiation it receives and the frequency of that radiation. Depending of the wavelength of the radiation it is possible to treat cancer or cause it, we can detect galaxies far away from us or see the microscopic world living inside us. For these reasons and many others the study of electromagnetic phenomena is indispensable in the toolbox of all the scientists. The potential applications of electromagnetic radiation is unlimited, this is why controlling light is a very attractive subject. From the physical point of view light is electromagnetic radiation which comprises electric and magnetic fields varying in time. According to the wavelength of the oscillation, the electromagnetic radiation can be generated in different ways and be used in different areas. Long wavelengths (10^7 nm – 10^{15} nm) are generated by electronic methods and are mostly used in communications (Transmission lines, TV, Radio, Phone).

Short wavelengths (10^{-4} nm – 10^6 nm) are used in many areas and more often in biomedical applications and are generated by quantum processes. In addition, for these short wavelengths a very interesting phenomena appears, the interaction of short wavelengths with matter is better understood assuming the light is a particle no a wave, this is one of the most beautiful result in physics and is called wave-particle duality. Between long wavelength and short wavelengths a gap in the electromagnetic spectrum exists, this is called de Terahertz (THz) gap (10^4 nm – 10^6 nm), shown in Fig1.1. This kind of radiation can not be generated by either electric or quantum methods. It was with the invention of the femtosecond laser that scientist were capable to have access to this gap. THz radiation has properties from both worlds, electronic and photonic. This is because why the study and manipulation of THz radiation is necessary. Most of the materials used in optical or microwaves devices are opaque for terahertz light but fortunately many polymers used in 3D printers are transparent in this band and the resolution of a convectional 3D printer ($400\mu m$) is enough for terahertz devices fabrication.

1.1 The terahertz gap

Terahertz radiation (THz) or sometimes called far-infrared radiation is radiation which lies in frequencies between 300 GHz and 10 THz ($30\mu m$ to $1000\mu m$). As seen in Fig. 1.1 these frequencies are between the microwaves and the infrared. But 30 years ago it was impossible to access to this region in the EM spectrum [1] because we did not have the appropriate technology. From the side of microwaves the velocity of the oscillation of the electron

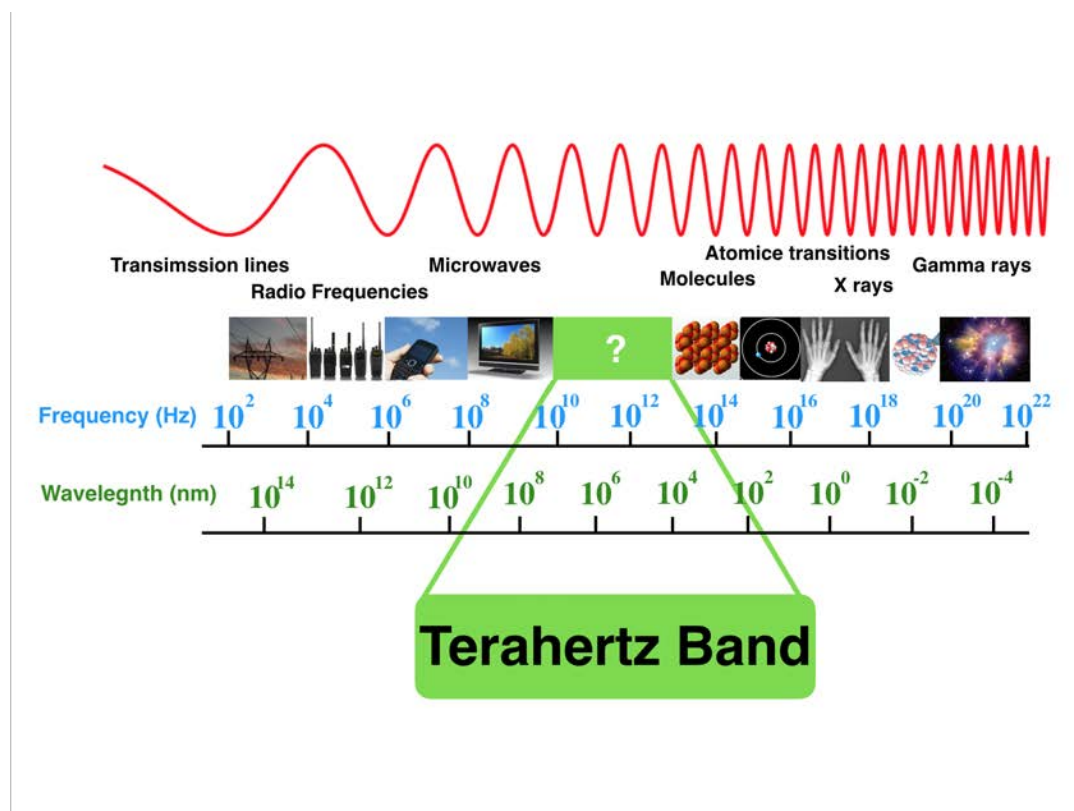


Figure 1.1: The electromagnetic spectrum. Bands of the spectrum are indicated from LF (low frequency) to cosmic rays as a function of their frequency ranges (also, scales in energy, wavelength and wavenumber units are given). Common sources of radiation are also shown for the different regions of the spectrum.

inside a typical transistor is limited by the size of the transistor and the voltage applied [2]. From the side of optics, it was not possible either because the temperature of one photon at 1 THz is 48 K (4.14 meV), while the room temperature is 298 K. Therefore the detection of terahertz radiation was only achieved using devices at cryogenic temperatures. In addition the energy of photons at THz frequencies can not excite electrons from the valence band to conductive band, because, in silicon, for example the band gap energy is around 1.1 eV and the energy of one photon at 1 THz is 1000 times lower than this value. In consequence it is impossible to use conventional photodiodes. It was with the invention of ultra-fast lasers that THz generation and detection was achieved using photoconductive antennas (PCA) [3]. Years later it was demonstrated the generation and detection of THz using optical rectification using non-linear crystals achieving bandwidths above 4 THz [4]. Later developments produced more efficient and devices resulting in the technique called Terahertz Time Domain Spectroscopy (THz-TDS) [5]. This technique has advantages over the other spectroscopy techniques (Raman, Infrared, etc.) because in this case the electric field is recorded, instead the power amplitude, resulting in the possibility to extract the complex refractive index of the samples [6, 7].

1.2 Terahertz time-domain-spectroscopy

In this section the basics of the THz-TDS technique are given. Nowadays there are many different methods for THz generation and detection, but in this thesis only the method of photoconductive antenna was used. TDS

systems generally use femtosecond laser pulses, these pulses have a temporal duration between 10 fs and 100 fs [8]. These laser pulses are generated through the mode-locking technique [5]. The laser cavity has an active medium capable to emit across different cavity modes simultaneously. Nevertheless, if the modes do not present a stable phase relation between them, the output radiation will fluctuate in a random manner around some average value. Yet, if the different modes present a linear phase relation between them, the output will be a train of well defined periodic pulses, in which the periodicity of the pulses is defined by the cavity length [1]. This is depicted in Fig. 1.2. In order to generate shorter pulses a broader emission bandwidth active medium is necessary in order to support more and more laser cavity modes. The most common active medium for ultrafast lasers is Titanium-Sapphire (Ti:Sapphire). This material has an emission bandwidth from 650 nm to 1,100 nm [9].

1.2.1 THz-TDS setup

The basic experimental setup for THz-TDS using photoconductive antennas is shown in Fig. 1.3. A near-infrared femtosecond pulse is divided by a beam splitter. One of this pulses is sent to the THz emitter in order to generate THz radiation. This pulse is known as pump pulse. The THz pulse is focused onto the sample using a pair of lenses (TPX, polyethylene or some other transparent material for THz radiation). One important fact is that the temporal duration of the THz pulse is around 1 ps approximately, this means the THz pulse is almost 100 times longer than the optical pulse (10-100 fs). The other half of the optical pulse, separated by the beam splitter, can be

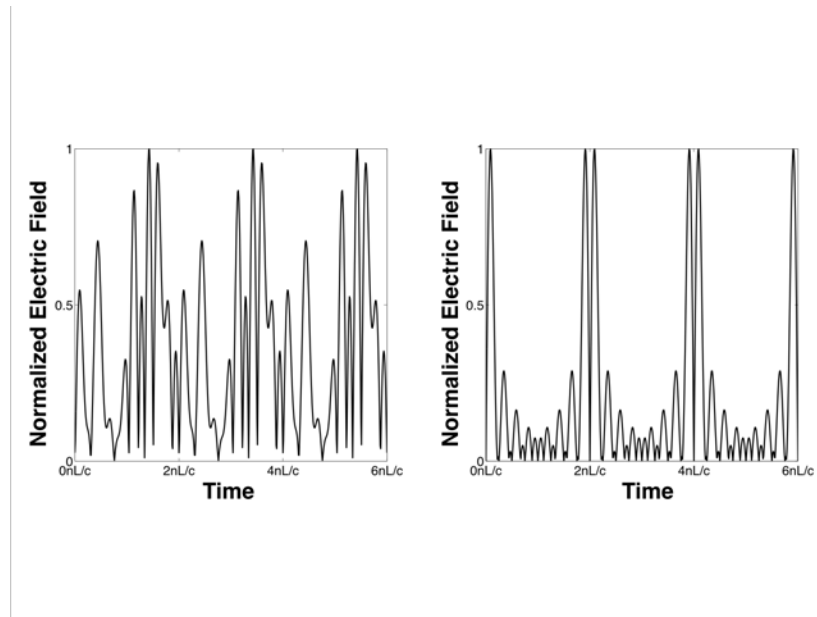


Figure 1.2: Laser pulses generated by a laser resonant cavity. The repetition rate of the pulses is $2nL/c$ where n is the refractive index of the material filling the cavity, L the cavity size and c the speed of light in vacuum. a) Sum of modes with no phase relation between them. b) Sum of modes when there are a linear phase relation between them. For this calculation eight modes were used.

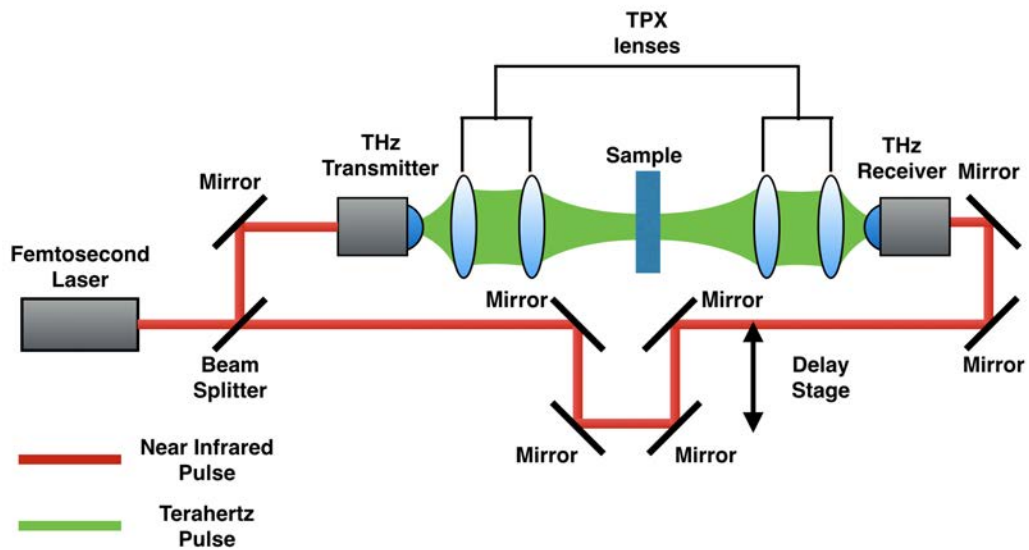


Figure 1.3: THz-TDS transmission setup. The femtosecond pulse (red line) is divided by a beam splitter and guided by a set of mirrors. One half of the original optical pulse is used for generating THz radiation (green) while the other half is used for the detecting process. The delay stage is used for overlapping the THz pulse with the optical pulse in different times.

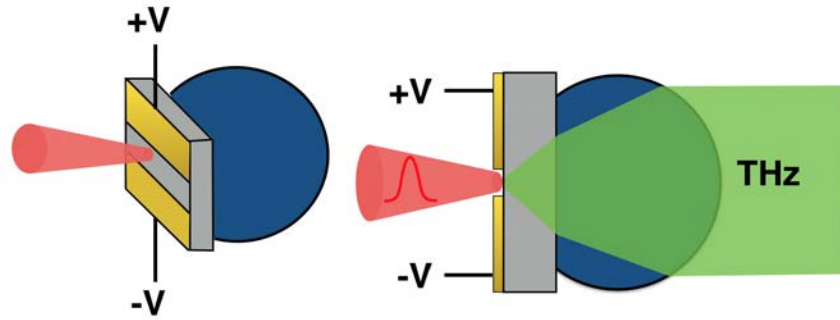


Figure 1.4: Photo conductive antenna (PCA). The antenna is fabricated using a semiconductor with a energy band-gap centered at the wavelength of the optical pulse. When the optical pulse hit the antenna, electron-hole pairs are created. The bias voltage across the antenna accelerated the charge-carrier pairs emitting THz radiation. The hyperemispheric lens behind the antenna is used to collimate the THz radiation.

used to sampling the THz pulse overlapping these two. This optical pulse is named probe pulse. The arrangement of Fig. 1.3 is typically know as free-space TDS because the optical pulse is traveling in free-space. New systems are fiber-coupled avoiding the use of mirror and making it easier to align. In the next section a brief explanation of THz generation and detection using photoconductive antennas is given.

1.2.2 THz Emission/Detection using PCAs

Nowadays there are many method for THz emission and detection [1]. In this section a explanation of the process using PCA is given. A simplified

diagram of PCA is shown in Fig.1.4 [1]. The antenna consists of a wafer of a semiconductor with energy band-gap near the wavelength of the optical pulse. On the semiconductor, a pair of electrodes are placed and connected to a bias voltage. For the emission process, the optical pulse is absorbed on the antenna between the electrodes generating electro-hole pairs. The recombination time of these pair can be from some nanosecond to few picoseconds [10] depending of the semiconductor. These carriers are accelerated by the bias voltage generating an electromagnetic transient. This transient radiation has frequency components in the THz band (0.05 THz-5 THz). For this work we used a fiber coupled Menlo systems spectrometer. The PCA was made of InGaAs and the separation between electrodes was around $10\ \mu\text{m}$. The excitation was made using a Er:Fiber with a pulse duration less than 90 ps and a repetition rate of pulses of 100 MHz with an average power of 60 mW.

It can be proved that in the far-field the THz pulse is given by [11,12]

$$E_{\text{THz}} \propto \frac{dI_{PC}(t)}{dt} \quad (1.1)$$

where E_{THz} is the THz electric field far from the emissor and I_{PC} is the generated photocurrent in the gap between electrodes.

The detection process is very similar to the generation process, there is not bias voltage across the antenna, instead, the antenna is connected in series to an amperimeter. Again overlap between the optical pulse and the THz pulse is necessary. When the optical pulse arrives to the gap in the antenna, it generates electron-holes pairs. These pairs are accelerated now

by the THz pulse. As was previously mentioned, the THz pulse is almost 100 times temporally longer than the optical pulse, it is because of this that in the overlap between pulses the optical pulse “see” a bias voltage with amplitude equal to the value of the intersection with the THz pulse. This charge acceleration gives place to a photocurrent which is measured with the amperimeter. The photocurrent is given by

$$J(t) = \int_{-\infty}^{\infty} E_{\text{THz}}(t')\sigma(t-t')dt', \quad (1.2)$$

where $J(t)$ is the photocurrent, E_{THz} is the THz electric field, t is the relative delay time between pulses and σ is the conductivity of the antenna induced by the femtosecond pulse given by

$$\sigma(t) = \text{erf}(t)e^{-t/\tau}, \quad (1.3)$$

where τ is the time constant. This constant in most cases is very short (some ps) and therefore σ is considered $\sigma(t) \approx \delta(t)$. The diagram of the detection process is given in Fig. 1.5

1.2.3 Applications of Terahertz radiation

Now having access to THz radiation, researchers have been able to study the interaction of this radiation with matter. The number of applications of this technology has in different fields like security [13], communications [14], biomedical imaging [15,16], molecular dynamics [17,18], etc. In the following paragraphs I present a list of the most important applications:

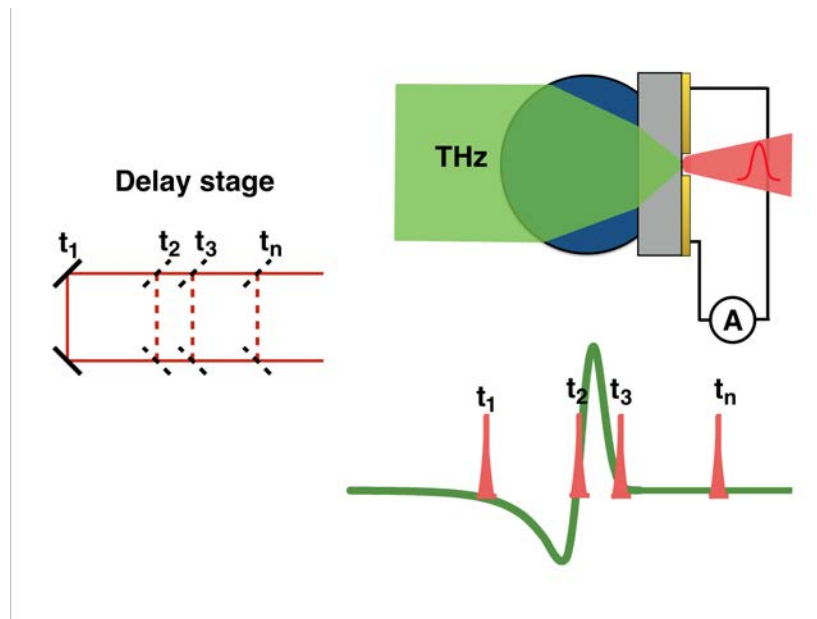


Figure 1.5: Photoconductive antenna (PCA) in detection configuration. The optical pulse hitting the gap between electrodes generates electro-holes pairs inside the semiconductor. These pairs are accelerated by the THz pulse generating a photocurrent. The amplitude of this photocurrent depends of the magnitud of the THz field in the intersection with the optical pulse. The photocurrent is measured with an amperimeter.

- Terahertz spectroscopy of crystalline and non-crystalline solids: Some spectral signatures of crystalline samples fall in the THz region, opening the possibility of recognizing of some substances or products like explosives, food additives or biomolecules [19]. Also, with this technique the extraction of the complex electrical conductivity is possible [20].
- Liquids and biomolecules: Terahertz radiation is very sensitive to the relaxation and collective motions of some molecules [21]. Some applications of this fact is the extraction of the amount of glucose, alcohol, oil and water content [22,23]. Using this technique it has been possible to find new vibrational modes in alcohols [24,25], as well as changes in the relaxation dynamics of some ionic liquids [26,27].
- Semiconductors: The dynamics of the charge carriers inside the semiconductors happens in periods of times between some nanoseconds to few femtoseconds and the study of it is possible with THz radiation [20,28,29]. These studies are called Pump-Probe experiments in which an additional beam splitter is used [30].
- Biomedical imaging: THz radiation is highly absorbed by water, then is possible to monitoring hydration and dehydration dynamics of biological samples in real time [31]. Also it is possible to find the complex dielectric function of biological samples giving place of skin cancer detection [32,33], tumors [34], dental cavities [35,36], etc. Fortunately, the energy of a photon at 1 THz is equal to 6.6×10^{-22} J or 4.1 meV. The necessary energy for ionizing an atom is 1,000 times larger. In conclusion THz radiation can be considered a non-ionizing radiation, then

the application of this radiation to biological systems is a possibility.

- Security imaging: Terahertz radiation can be used to image dangerous objects, such as guns, drugs and explosives, this because these objects have a particular dielectrical response in the THz band [13]. With this signature THz radiation can be used in airports as a non-invasive test [37].
- Cultural heritage: Many pigments used in artistic paintings are transparent to THz radiation. This radiation can be used as a non-invasive and non-destructive technique for the evaluation of the deterioration of various forms of artworks [38, 39]. In addition some of these pigments have spectral signatures in the THz band, therefore the pigment recognition in the THz band is possible [40–42].

1.3 Objectives of this work

In this thesis four new quasi-optical devices for the THz band are shown. Three of them were 3D printed and the last one is based on an artificial dielectric made of metallic parallel-plate-waveguide (PPWG). In Chapter 2 an introduction to the fundamentals of the 3D printing process is given in addition to a brief introduction of gcode generation. Chapter 3 shows to the best of our knowledge the first 3D printed GRIN lens. These new low-cost lenses were tested using THz time-domain spectroscopy and imaging in order to measure their optical properties. The results show a focusing capacity within the diffraction limit for frequencies below 700GHz.

In Chapter 4 the fabrication and characterization of 3D printed quasi-Wollaston prism (polarization splitter) based on form birefringence is shown. The prism uses the birefringence induced in a sub-wavelength layered plastic-air structure that produces refraction in different directions for different polarizations. The component was simulated using the finite-difference-time-domain method, fabricated by 3D printing and subsequently tested by terahertz time-domain spectroscopy showing a polarization separation around of 23° for frequencies below 400 GHz, exhibiting cross polarization power extinction ratios better than 1.6×10^{-3} at 200 GHz.

Chapter 5 shows the first 3D printed terahertz q-plate with continuous birefringence variation at terahertz frequencies. This birefringence is also produced using form birefringence. This q -plate was fabricated by three-dimensional printing and is a simple solution for the generation of cylindrical vector beams. This device can find a number of applications in future terahertz technologies such as telecommunications.

Finally in Chapter 6 we theoretically and experimentally demonstrate a stepped- refractive- index convergent lens made of a parallel stack of metallic plates for terahertz frequencies based on artificial dielectrics. The lens consist of a non-uniformly spaced stack of metallic plates, forming a mirror-symmetric array of parallel-plate waveguides (PPWGs). The operation of the device is based on the TE_1 mode of the PPWG. The effective refractive index of the TE_1 mode is a function of the frequency of operation and the spacing between the plates of the PPWG. By varying the spacing between the plates, we can modify the local refractive index of the structure in every individual PPWG that constitutes the lens producing a stepped refractive

index profile across the multi stack structure. The theoretical and experimental results show that this structure is capable of focusing a 1 cm diameter beam to a line focus of less than 4 mm for the design frequency of 0.18 THz. This structure shows that this artificial-dielectric concept is an important technology for the fabrication of next generation terahertz devices.

Chapter 2

Three-dimensional printing

Three-dimensional printing or additive manufacturing (AM) is a rapidly developing technology because of its ability to create very fast and very economical elements for various purposes, including prototyping [43]. For this reason this technology is sometimes called rapid prototyping (RP). In this technique the object is created by adding layers of material from the bottom, until the object is formed. In Fig. 2.1 a simplified diagram of a 3D printer is given in order to understand how it works.

3D printing is only one method of additive manufacturing. Additional methods are: stereolithography, inkjet printing, selective laser sintering, binder printing among others. A complete compendium of these techniques, examples, listing benefits, how they work, important characteristics of each and materials used can be found in [44].

In contrast to traditional mechanical machining, or subtractive manufacturing (SM), additive manufacturing, has several benefits. One of the most important ones is that the amount of material required is less than in

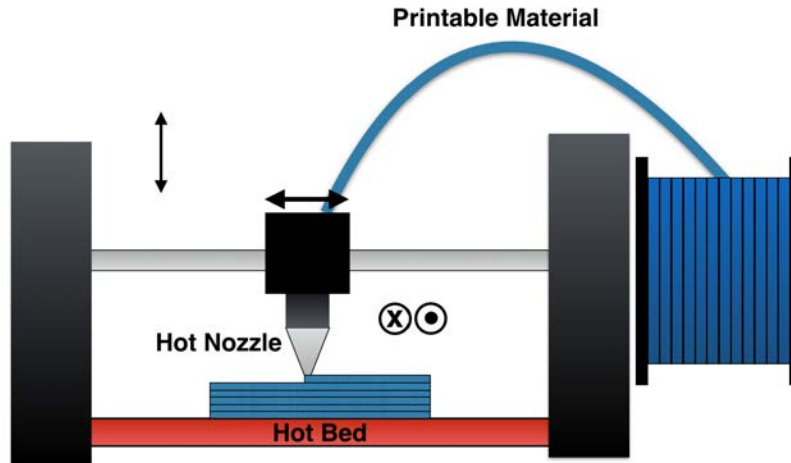


Figure 2.1: 3D printer diagram. The 3D printer reads the CAD code and builds the object layer by layer adding small amounts of the printable material. In some cases a hot bed is necessary in order to improve the quality of the printed object.

subtractive manufacturing. This is because only the amount of material necessary for the construction of the object is used on the contrary of SM where material is removed from a block until the object is fabricated. Another advantage is the broad spectrum of materials used in AM. These materials can be used from industrial proposes to biomedical applications [43].

2.1 General steps of the 3D printing process

The general process of 3D printing involves the printer and some modeling software (CAD) that is used to define or design the geometry of the object produced. In this thesis we bypassed the use of CAD by using mathematical softwate (Phyton, Octave, Matlab). This is necessary in order to precisely control the path and the velocity of the 3D printer. Later in this chapter the

geometry generation using Matlab is shown.

In the second step and after the CAD representation is achieved, it is necessary to transform the file into a STL file. The STL format is a raw triangulation of the object and form the basis calculation of the slices. In Fig. 2.2 an example of CAD to STL transformation is given.

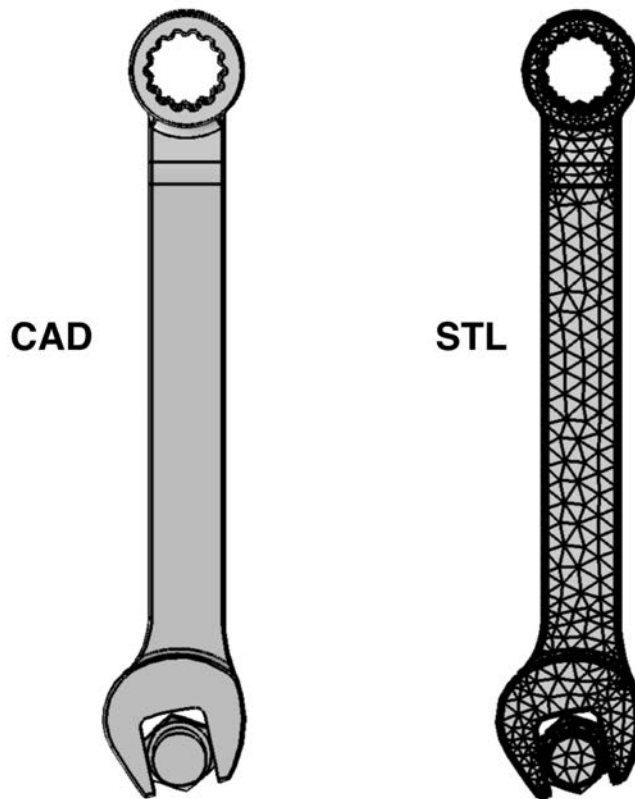


Figure 2.2: Comparison between CAD and STL file. In CAD only the representation of the object is given without any trajectory of building. On the contrary STL file is a triangular representation of the object, giving the triangle vertices. This information is the basis of the trajectory calculations.

The next step in the process is processing the STL file in order to transform it into a G-code. This step converts the triangulation of the STL file into instructions to be executed by the printer, which are basically a sequence of x , y and z coordinates, plus an additional coordinate that controls the mate-

rial injection. In this process many optimization algorithms are used in order to find the most efficient path for the construction of the object. Unfortunately this process is limited because as a user, it is not possible to choose the path of construction of the object. For example in electromagnetic or optical component fabrication it is necessary to follow a particular trajectory in its building process in order to minimize some undesired effects such a diffractive effects, scattering, etc. In order to fabricate the components that will be presented in the following chapters complete control is achieved by using Matlab. This will be discussed in the next sections.

Inside the G-code there is not only information of the geometry the object to be built, but information about the printer settings is also present. Such information includes nozzle temperature, bed temperature, position of the stepped motors, where is the origin of coordinates, speed of the printer, amount of material extruded, fan turn on when the temperature threshold reaches certain value, among others. Fig. 2.3 summarizes the printing process

The structure in which the information is ordered in the G-code file can be summarized in three blocks:

- General information of the setting: Nozzle temperature, bed temperature, turning on the stepped motors, physical dimensions of the numbers in the file, checking the origin of coordinates, starting all stepped motors at 0, starting the fan, some legend if the printer has a display, among others.
- Trajectory followed by the nozzle. This is the most important part for this work, because in this part of the file the operator can choose

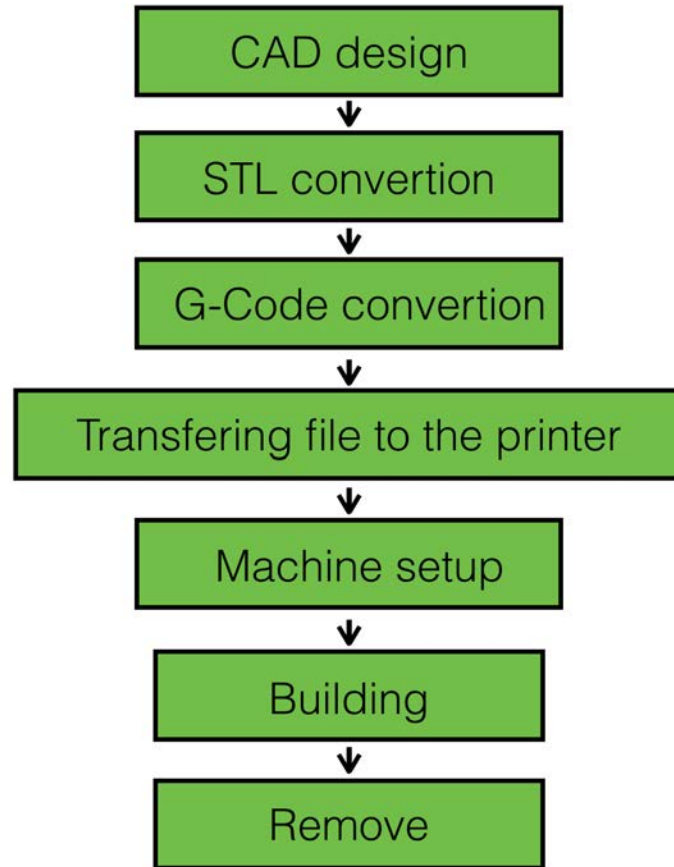


Figure 2.3: Summary of the 3D printing process.

the trajectory that the nozzle will follow is defined. This part can be modified using any mathematical software like, Python, Octave, Matlab, etc. or even a text editor.

- Turning off all the components: fan, motors, heater of the nozzle and bed, returning the nozzle to the origin.

The first and third block show very few, if any, variations between pieces, unless the operator wants to change the initial setup. Knowing this, in this work we generated a txt file following the order of those three block but

modifying the second block in order to choose a smart trajectory for our object. By generating the G-code directly using this method it is possible to avoid the CAD design step and the STL conversion and to have a full control over the fabrication strategy, which is important for the kind of devices I report in this thesis. Fig. 2.4 is an example of a generic g-code header and footer. For this work we used a Prusa i3 3D printer from makermex. In Fig. 2.1 a picture of the printer is shown. The resolution of our printer was $400\ \mu\text{m}$ limited by the nozzle hole diameter. The price of this printer is accesible for any research lab and many aspects of this apparatus are customizable.

Header	Footer
M190 S70.000000 (bed temperature)	M107 (fan off)
M109 S230.000000 (nozzle temperature)	G0 F9000 X # Y # Z # (end position)
G21 (metric values)	M104 S0 (extruder heater off)
G90 (absolute positioning)	M140 S0 (heated bed heater off)
M82 (set extruder to absolute mode)	G91 (relative positioning)
M107 (start with the fan off)	G1 E-1 F300 (retract the filament a bit before lifting the nozzle, to release some of the pressure)
G28 X0 Y0 (move X/Y to min endstops)	G1 Z+0.5 E-1 X-20 Y-20 F9000 (move Z up a bit and retract filament even more)
G28 Z0 (move Z to min endstops)	G28 X0 Y0 (move X/Y to min endstops, so the head is out of the way)
G1 Z10.0 F9000 (move the platform down 15mm)	M84 (steppers off)
G92 E0 (zero the extruded length)	G90 (absolute positioning)
G1 F200 E3 (extrude 3mm of feed stock)	
G92 E0 (zero the extruded length again)	
G1 F90 (Printing speed mm/seg)	
M117 Printing... (Screen display)	
M107 (fan on)	
[G0 F9000 X' # ' Y' # ' Z #'] (starting position)	

Figure 2.4: Typical header and footer for G-code. Between these two the trajectory of object to build need to be placed.

2.2 Terahertz applications of 3D printing

As stated in the previous chapter terahertz radiation has become a powerful tool for a number of scientific and real-world applications. Therefore devices to manipulate radiation in this spectral band are in growing demand. Unfortunately many materials, transparent in the visible range, are opaque at terahertz frequencies. Previous studies demonstrate that many 3D-printable polymers are transparent at terahertz frequencies [56]. Three dimensional printing has gained attention owing to its capability of rapidly producing prototypes of objects with complex geometries that can easily be computer designed. Furthermore, users of this technology can easily produce programs in order to directly control the motion of the printer which allows them using the full capacity for the production of components with resolution-limited features. Typically, the resolution of a fused-polymer-injection printer is around $400\ \mu\text{m}$. This resolution was proven to be good enough to make THz devices appropriate for frequencies below $\sim 800\ \text{GHz}$. Examples are, lenses and gratings [56, 57], terahertz optical fibers [58, 59], grin lenses [60, 61], zone plates [62] and waveguides [63–65].

Chapter 3

3D printed GRIN lens

In this section we report on the fabrication of gradient-refractive-index (GRIN) THz lenses using a 3D printer. The GRIN lenses were made out of polystyrene, because it is a 3D-printer-compatible highly transparent material in the THz regime [56]. The performance of the GRIN lenses were characterized using THz-TDS and imaging. The results demonstrate 3D printing technology is a new promising technique for the fabrication of complex low cost THz components.

The idea behind the GRIN lenses we propose is using a structure that mixes polystyrene and air in order to produce an effective medium with a controlled refractive index that can be varied by design.

Two-dimensional finite-difference-time-domain simulations were performed in order to identify the performance of the structure [66]. A plane wave was propagated by our simulation through a column of material slabs of length 2.5 mm and width 400 μm . The spacing between slabs changes linearly as a function of the distance to the optical axis ($x = 0$). Fig.3.1 a) and b)

show the results of the simulation for 375 GHz ($\lambda = 800 \mu m$) and 750 GHz ($\lambda = 400 \mu m$) for a plane wave with polarization parallel to the stacks of material. The simulation for $800 \mu m$ shows the behavior typical of a standard lens, demonstrating that the concept behind our GRIN lens works correctly. For the case of $400 \mu m$ the behavior is not ideal, showing a longer focal length together with some diffraction, caused by the features of the structure being comparable to the radiation wavelength, in other words, for wavelengths longer than the structure features, the structure behaves well as an effective medium, unlike for wavelengths comparable or longer to the features of the structure. Fig. 3.1 c) and d) show simulation results analogous to the ones shown in a) and b), the only difference is the polarization vector of the plane wave, which is perpendicular to the stacks of material. The simulations shows a similar behavior no matter what polarization the plane wave has. The small perturbation appearing for $z < 0$ are caused by the radiation reflected from the GRIN structure.

In order to explain the reason for our specific design it is important to understand the fused material deposition method used by our printer. We do not aim to give an exhaustive explanation here, but we want to give a brief description to the reader. The base of the printer is a heated nozzle with a motor that injects polymer into it at a controlled rate. This entire piece is called the extruder. The polymer melts in the nozzle and the melt flows through a small aperture in the nozzle, which in our case is $400 \mu m$ in diameter, producing a thin filament ($\sim 400 \mu m$) of material. The extruder can be moved in two dimensions over a flat bed where the filament is deposited and cools down in order to solidify again. By controlling the position

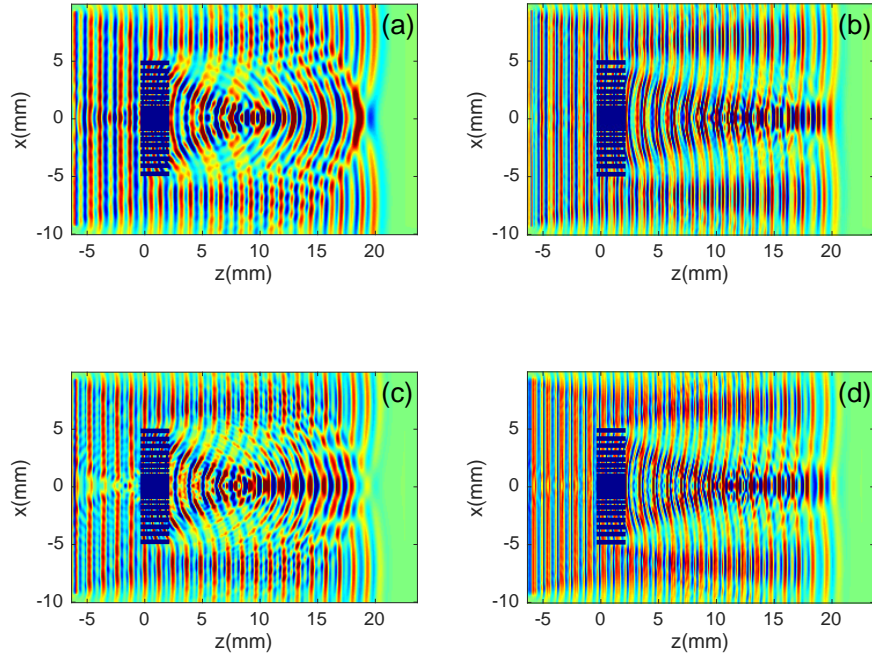


Figure 3.1: Two dimensional electromagnetic simulation of GRIN lenses made of a stack of $400\ \mu\text{m} \times 2.5\ \text{mm}$ material slabs ($n=1.55$) with increasing spacing as a function of the distance to the optical axis ($y=0$). a) Shows a plane wave with linear polarization parallel to stacks of material of frequency 375 GHz ($800\ \mu\text{m}$) is simulated, the stack of material slabs is shown at $z=0$, the simulation shows a clear focal point at $z \sim 10\ \text{mm}$ typical of a lens. b) Shows a plane wave with linear polarization parallel to stacks of material of frequency 750 GHz ($400\ \mu\text{m}$) with a focal distance of $z \sim 15\ \text{mm}$. c) and d) Are analogous to a) and b) but with the polarization perpendicular to the stacks of material.

of the extruder and the material injection rate it is possible to produce a layer with almost any desired structure. The bed is subsequently lowered by certain amount, typically $\sim 100 \mu\text{m}$, and a new layer is deposited on top of the previous one, that way a three dimensional object can be built [67].

Aiming to produce a lens with a usable bandwidth as large as possible we thought that the design should use the smallest printable feature that our 3D printer could produce, i.e. the above mentioned $400 \mu\text{m}$. Such feature is limited by the width of the printer's nozzle diameter used to deposit the molten polymer on the printed piece. Complicated structures incorporating holes or other discontinuous features of such small diameter are extremely hard to print with reasonable quality, given that it implies stopping and starting the flow of polymer over the printing trajectory of each layer. Therefore, we decided to aim for a structure that could be printed with a continuous injection of material in a soft and continuous trajectory. This led us to using stack of spiral layers for which the radius varies in a controlled manner in order to leave an increasing air separation for each turn of the spiral. Such spacing can be controlled in order to produce the desired effective refractive-index-gradient as shown in Fig. 3.2

The specific trajectory used is described by the polar equation

$$r(\theta) = r_0 \left(1 + \frac{\theta}{2\pi} \right) + m_{\text{air}} \frac{r_0^2}{r_l} \left(\frac{\theta}{2\pi} \right)^2, \quad (3.1)$$

where $r_0 = 400 \mu\text{m}$ is the nozzle hole diameter, m_{air} is the volumetric fraction of air at the edge of the lens, which is at radius r_l . m_{air} is defined as t/h , where t and h are the spiral thickness and the space between the last spiral

line and the previous line, respectively, as shown in the inset of Fig. 3.2. The first term of the equation produces a spiral whose radius varies at a rate of $400\ \mu\text{m}$ per turn, namely, it would produce a solid spiral of material. The second term is an addition that increases the radius by an amount that grows linearly as a function of the angle in order to have an increasing gap of air as the angle and radius increases, starting with a solid material in the central part of the spiral. The final structure is a stack of such spirals. The effective medium resulting from the material and air combination produces an object with a refractive index that varies as a function of the radius, namely a GRIN lens. We made six different lenses, each with $m_{\text{air}}=0.2, 0.3, 0.4, 0.5, 0.6$ and 0.7 , named L2, L3, L4, L5, L6 and L7 respectively.

3.1 Experimental setup

A typical TDS system [47] was mounted in transmission geometry as show in Fig. 3.2 b). The lens closer to the emitter was replaced by a GRIN lenses. Two types of measurements were made in order to characterize the focal performance of the GRIN lens, transverse and longitudinal measurements. Images of the vicinity of the focal point were performed by apperturing the optical path with an iris mounted on a two-dimensional stage as show in Fig. 3.2 b). A full time-domain waveform was recorded for each position of the iris. In the transverse measurement, we imaged the focal point and in the longitudinal measurement we determined the focal distance and the depth of focus. For the transverse measurement the translational stages are setup to move in the xy plane as show in Fig. 3.2 b). The radiation that

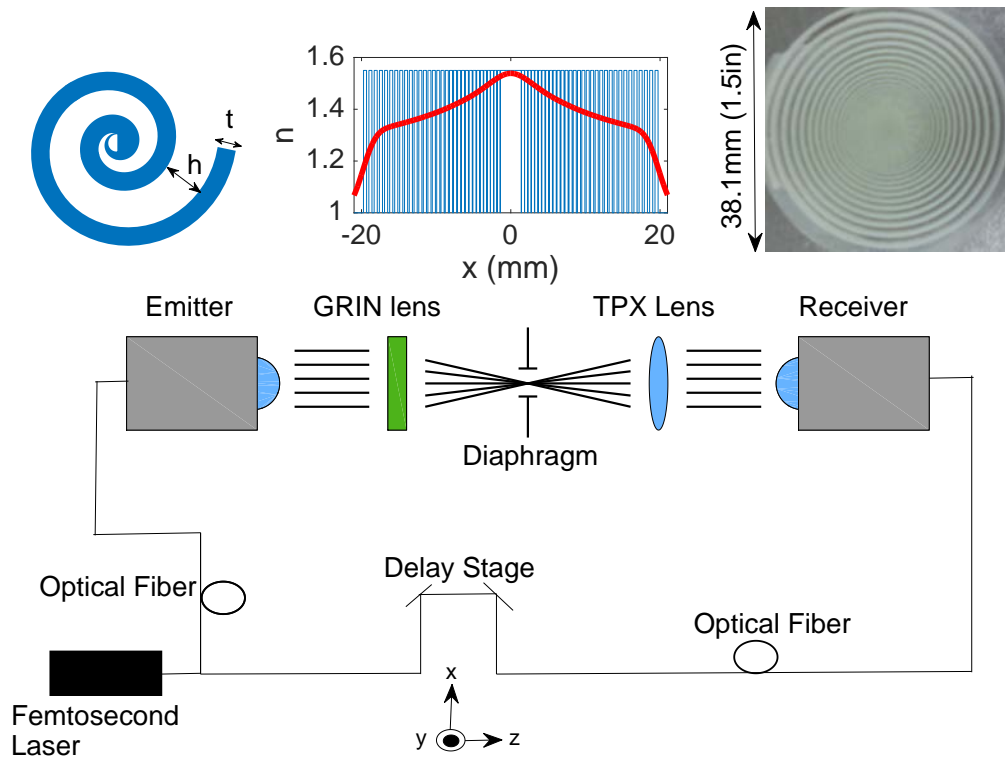


Figure 3.2: The top left-hand-side inset is a schematic representation of the lens structure design. The centre shows a plot of the transverse refractive index profile (thin line) and the effective refractive index that results from the structure (thick line). The right-hand-side inset is a photograph of the finished lens. The experimental setup is shown at the bottom. For the transverse measurements, a diaphragm is mounted on a pair of translational stages moving in the xy plane (at the focal plane), the radiation passing through the diaphragm at each position of the iris is recorded by the detector. For the longitudinal measurements, the diaphragm moves in the yz plane.

pases through the aperture is recorded by the receiver for each position of the aperture across a two dimensional grid of positions. In similar fashion, the longitudinal measurements, the stages move on the yz plane.

3.2 Results

3.2.1 Transverse measurements

We imaged the cross-section of the six GRIN lenses, yet, for clarity we will discuss in detail the samples with least (L2) and most (L7) refractive index gradient only. The intensity at 400 GHz is shown in Fig. 3.3 a) and b). In order to calculate the full-width-at-half-maximum (FWHM) in the x and y direction, two gaussianans were fit to the data for $x = 0$ and $y = 0$. In order to characterize the performance of the lenses quantitatively, we show the frequency dependent cross-section of the focal point for L2 Fig. 3.3 c) and L7 Fig. 3.3 d). The dashed lines in each panel represents the FWHM of an Airy disk at each frequency. As seen in the figure, the focal point produced by both lenses is diffraction limited, at least up to 700 GHz, where the signal is no longer visible in the plot.

3.2.2 Longitudinal measurements

With the longitudinal measurements we can obtain the focal distance and the focal depth for every GRIN lens. The measurements for depth of focus are show in Fig. 3.4 a) and 3.4 b) at 400 GHz. As expected, the focal length is longer in the L2 lens than in L7 because the effective refractive-index-gradient

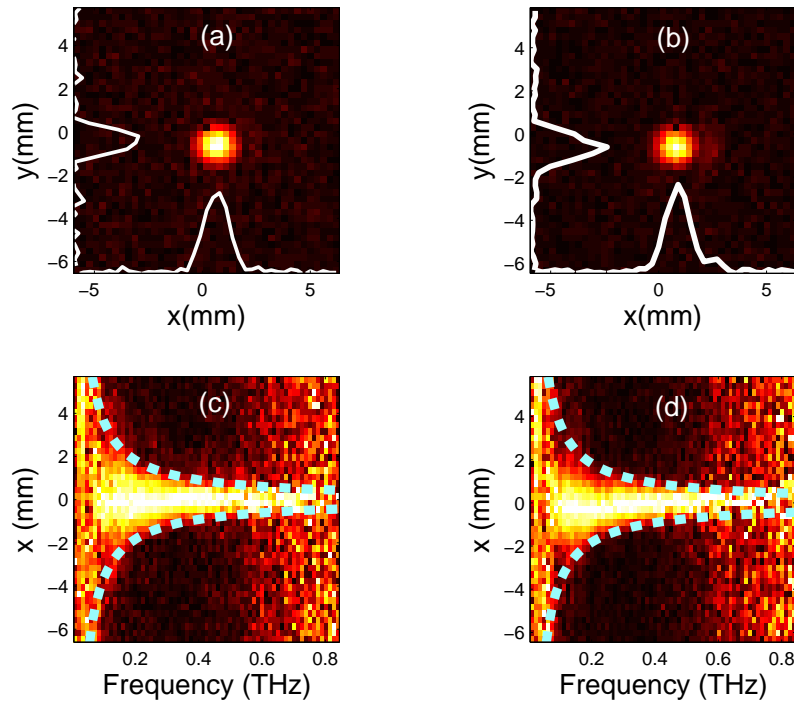


Figure 3.3: Transverse amplitude measurements. a) and b) shows the cross-section of the focal point for L2 and L7 respectively. For a frequency of 400 GHz the lines are the central cuts. c) and d) show the corresponding frequency dependence of the focus' cross section. The dotted lines represent the theoretical size of the Airy disk, showing good agreement with the measurements.

Table 3.1: Summary of transversal and longitudinal measurements at 400 GHz

Lens	Focal distance (mm)	FWHM _x (mm)	FWHM _y (mm)
L2	40	1.86	2.21
L3	55	1.86	2.13
L4	42	2.01	2.10
L5	43	2.18	2.13
L6	31	2.16	1.96
L7	18	1.49	2.05

in L2 is higher than in L7. Given that the effective refractive-index-gradient was produced in the lenses by a structure that has features of dimensions comparable to the THz wavelengths we expect that each frequency presents a different focal distance. In order to quantify this chromatic aberration, we take a central cut in the longitudinal waist measurement for every frequency in order to see how the focal distance changes as a function of frequency. The results for the L2 and L7 lenses are show in Fig. 3.4 c) and 3.4 d). In order to have a better visualization we show a dashed line over the maximum amplitud at every frequency as a “guide to the eye” in order to see the trend of the focal position. The slope of this line is an indication of the chromatic aberration. The results for the transverse and longitudinal measurements of all the lenses are summarized in Table 3.1

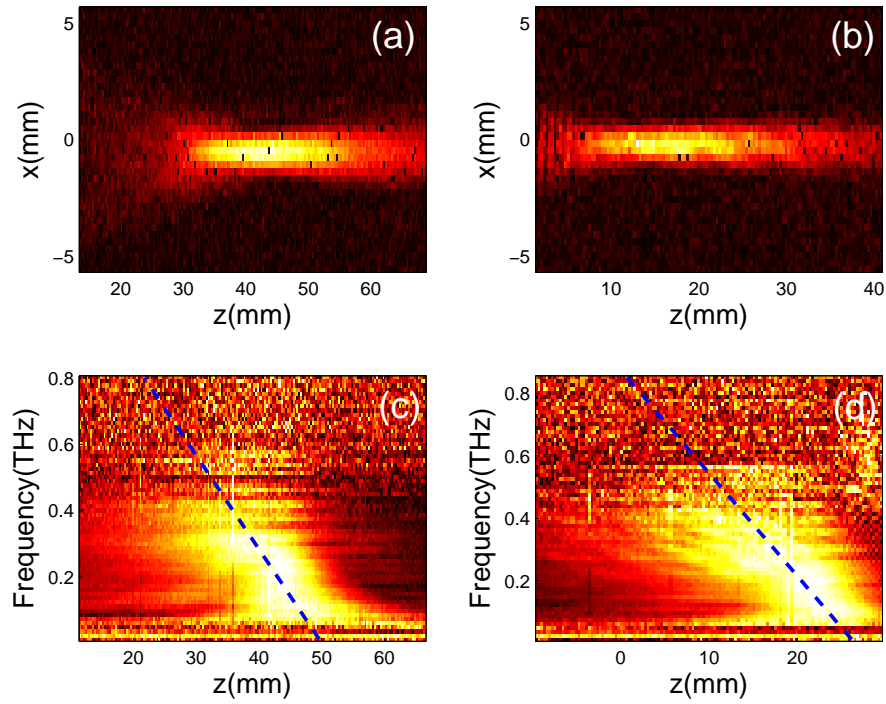


Figure 3.4: Longitudinal amplitude measurements. a) and b) shows the beam waist and depth of focus at 400 GHz. c) and d) are the amplitude as function of the longitudinal position and the frequency and the inserted line is a fitted line in order to quantify the chromatic aberration through its slope.

Chapter 4

3D printed polarization splitter

In this section we use 3D printing in order to make a polarization splitter, similar to a Wollaston prism, using form birefringence [68]. Firstly the design was modeled using a finite-difference-time-domain simulation [66]. The device was printed and subsequently tested using a terahertz time-domain spectroscopy system. The experiments demonstrated apolarization around 30° for frequencies below 400 GHz.

4.1 Device design and modeling

In order to make the polarization splitter we induce form birefringence by building a layered structure that combines air and Bendlay. The device was fabricated using a Prusa i3 printer with a $400\mu\text{m}$ nozzle which determines its resolution. Firstly we made a sample with $d = 400\mu\text{m}$ -thick walls of Bendlay ($n=1.53$ below 1 THz) with period of $\Lambda = 800\mu\text{m}$ [56]. This structure is schematically shown in the inset of Fig.4.1. The solid lines in Fig.4.1 are

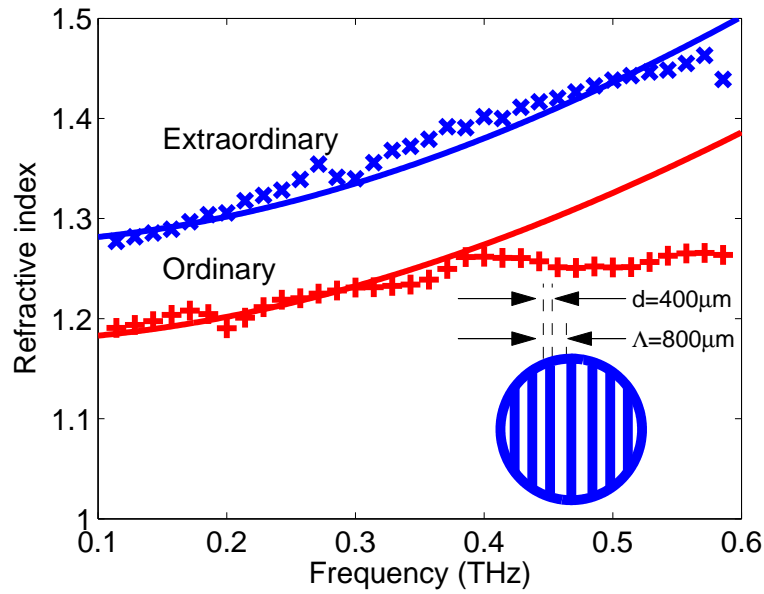


Figure 4.1: Ordinary (perpendicular to the layers) and extraordinary (parallel to the layers) refractive indices of the birrefringent structure. The continuous lines are the predicted refractive index for the two orthogonal orientations and the tilted crosses and crosses are experimental measurements. The curves agree for frequencies below 400 GHz. Inset shows the form-birrefringent structure used for this characterization.

the predicted refractive indices for such structure [68], given by

$$n_e^2 = n_{\parallel}^2 + \frac{1}{3} \left[\frac{\Lambda}{\lambda} \pi f_1 f_2 (n_1^2 - n_2^2) \right]^2 \quad (4.1)$$

and

$$n_o^2 = n_{\perp}^2 + \frac{1}{3} \left[\frac{\Lambda}{\lambda} \pi f_1 f_2 \left(\frac{1}{n_1^2} - \frac{1}{n_2^2} \right) n_{\parallel} n_{\perp}^3 \right]^2 \quad (4.2)$$

where Λ is the structure period, λ is the wavelength, $n_1 = 1.53$ and $n_2 = 1$ are the refractive indices of the layers, f_1 and f_2 are their respective volumetric fractions,

$$n_{\parallel}^2 = f_1 n_1^2 + f_2 n_2^2 \quad (4.3)$$

and

$$n_{\perp}^2 = \left(\frac{f_1}{n_1^2} + \frac{f_2}{n_2^2} \right)^{-1}. \quad (4.4)$$

The two refractive indices of the material were measured using terahertz time-domain spectroscopy with linearly polarized pulses parallel and perpendicular to the material layers of the sample and the analysis was performed as described in [68]. The tilted crosses and crosses in Fig. 4.1 are the experimentally measured refractive indices for the ordinary and extraordinary polarizations. The measurements are in acceptable agreement with the theoretical predictions for frequencies below 400 GHz. The discrepancy for higher frequencies can be attributed to the fact that higher frequencies (shorter wavelengths) are comparable or shorter to the features of the structure, which in turn produces diffraction and guiding in the layers, which are highly anisotropic and are not considered in the model used for the solid lines.

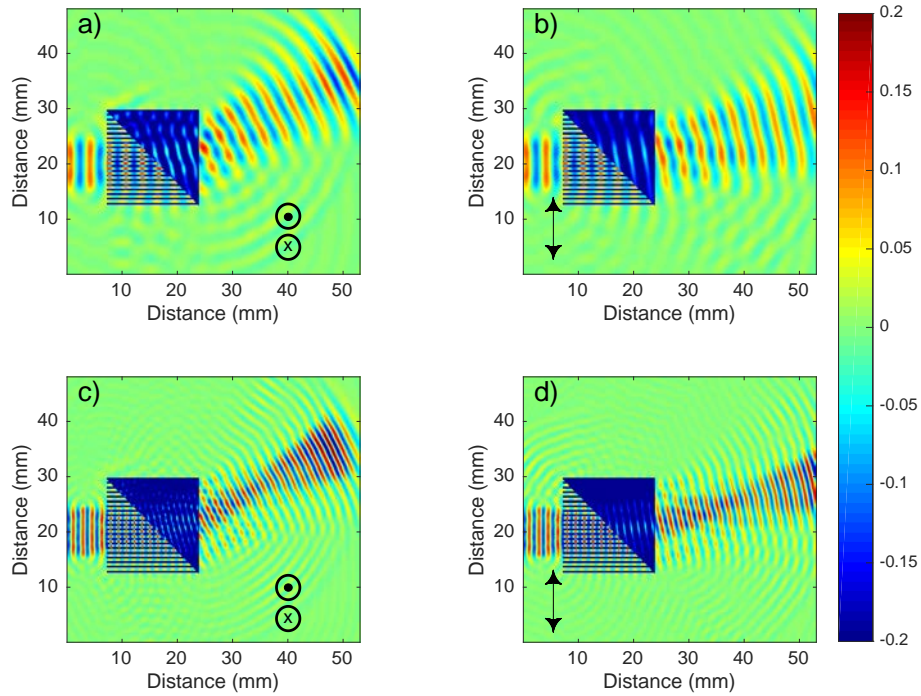


Figure 4.2: Electric field calculated by finite-difference-time-domain simulation for the device proposed. The Wollaston prism was made of $400 \mu\text{m}$ spacing $n=1.0$ and parallel walls $n=1.53$, valid below 1 THz, in a triangular configuration and a solid prism of the same material. a) and b) show simulation results for polarizations parallel and perpendicular to the layers respectively with an incident plane wave at 100 GHz. c) and d) show the analogous simulations to a) and b) at 600 GHz. The deflected angles are approximately 29° and 11° for the polarization parallel and perpendicular respectively

The geometry we propose for the quasi-Wollaston prism is schematically shown in Fig. 4.3a. This component is a cubic object with a layered structure in one half of it, similar to the one used for the form birefringence characterization, and solid material in the other half. The two halves meet at a 45° angle forming a component similar to a Wollaston prism. We simulated such structure using a finite-difference-time-domain model. The results for the two polarizations at 100 GHz are shown in Fig. 6.2a and b respectively. The colourmaps show that the radiation is refracted at the 45° interface at considerably different angles remaining relatively collimated after propagating through the entire structure. Similar simulations are presented in Fig. 6.2c and d for 600 GHz. In this case the beams for the two polarizations are still deflected at different angles, but the radiation does not remain collimated and a more complex diffraction structure appears. The deflected angles are 29° and 11° for the polarization parallel and perpendicular respectively

4.2 Experimental setup

In order to test our device, we used a Menlo system Tera K15 fiber coupled spectrometer in transmission configuration. The radiation was produced in an InGaAs photoconductive emitter, and two TPX lenses were used to collimate and focus the radiation on the sample. Two additional TPX lenses and an InGaAs photoconductive detector were mounted on a mobile arm driven by a computer controlled rotational stage in order to measure terahertz waveforms as function of the angle as shown in Fig. 4.3 b.

The device was fabricated by 3D printing with Bendlay ($n=1.53$ below

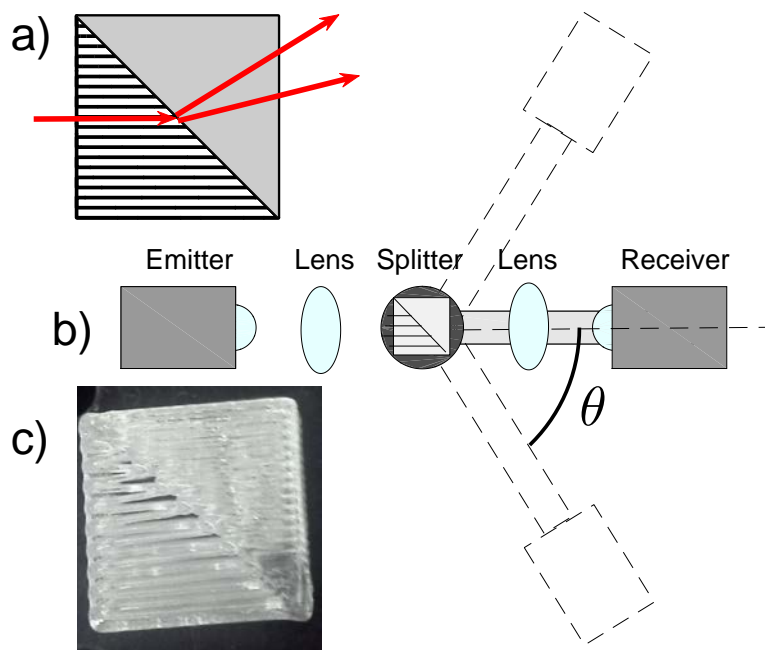


Figure 4.3: a) Schematic representation of the proposed structure indicating where the separation of polarizations occur. b) Experimental setup. One half of the system was fixed on the table while the other half was mounted on a rotatory stage in order to take measurements at angles ranging from -90° to 90° , being 0° the straight position through the emitter, in order to detect the deflected radiation by the device which remained fixed in the center. c) Picture of the fabricated device.

1 THz). The device is a cubic structure of 2 cm side with a layered structure in one half and a solid material in the other. The two halves meet at a 45° angle with respect to the cube walls. In order to test the device it was mounted at the sample position and remained fixed. Waveforms were recorded for angles between -90° and 90° in 1° steps, where 0° corresponds to the optical axis in the absence of the prism. The emitter and detector were first placed so that the radiation was produced and detected with polarization perpendicular to the layered structure, and subsequently the experiment was repeated with the emitter and detector rotated so that radiation had polarization parallel to the layered structure.

4.3 Results

After acquiring the data sets for the two polarizations, each waveform was Fourier transformed. The radiation patterns for the polarization parallel (continuous) and perpendicular (dashed) to the birefringent structure walls as a function of the angle are shown in the polar plots in Fig. 6.4a, b, c and d for 100 GHz, 200 GHz, 300 GHz and 400 GHz respectively. These plots show that the radiation polarized perpendicular to the structure was deflected about 30° , while the one parallel was deflected about 0° . The 100 GHz and 400 GHz plots show a complex structure of the patterns, being poor signal-to-noise ratio and diffraction the reasons respectively. In order to have a better picture, the angle and frequency dependent amplitude of the two polarizations are shown as colormaps in Fig. 6.4e and f. These plots confirm that the radiation is deflected at around 28° and 0° all across the spectrum and

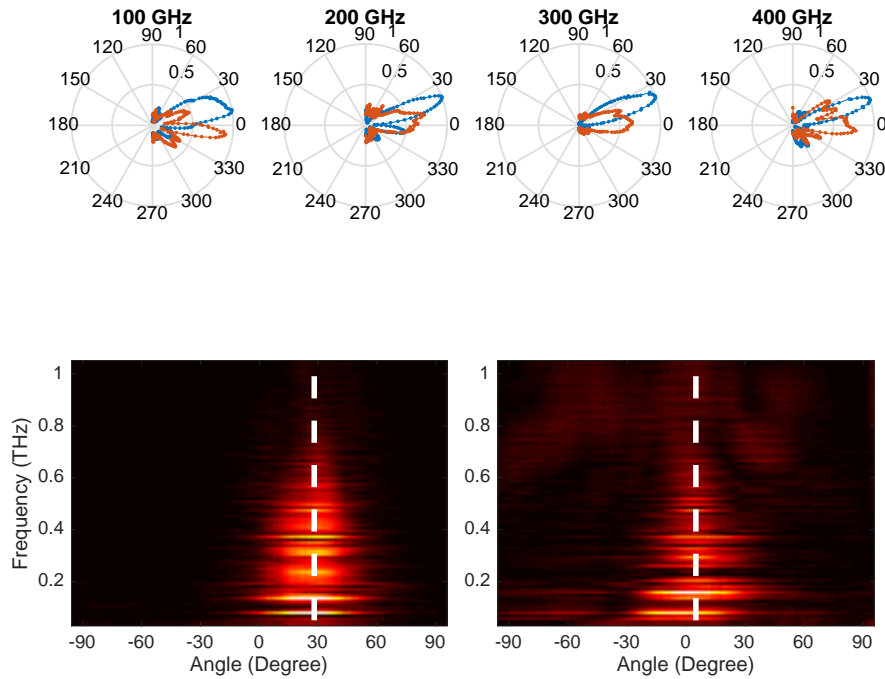


Figure 4.4: Radiation patterns at different frequencies after propagation through the device. The red dotted lines are radiation with polarization parallel to the structure layers and the blue dotted lines are radiation with polarization perpendicular to the layers. For frequencies between 200 GHz and 300 GHz the radiation is well separated for the two polarizations. For 100 GHz and 400 GHz the radiation was spread or overlapping. At the 100 GHz the signal to noise ratio in the spectrometer was poor but polarization separation remains. At 400 GHz the features of the structure are in the order of the wavelength. e) and f) are the deflected angle at every frequencies for polarization perpendicular to the material layers and parallel to the material layers respectively. The discontinuous lines are lines at 28° and 5° as a guide to the eye.

that additional diffracted “orders” with smaller amplitude appear at angles larger than 50° at frequencies higher than 400 GHz. The discontinuous lines are lines at 28° and 5° as a guide to the eye.

The device showed an electric field amplitude (power) cross polarization extinction ratio of 0.02 (4×10^{-4}) and 0.04 (1.6×10^{-3}) for the parallel and perpendicular components respectively at 200 GHz. In addition the transmittance for the parallel and perpendicular components were 0.23 and 0.24 respectively also at 200 GHz.

Chapter 5

3D printed q-plate

A q -plate is a birefringent wave plate with a space-dependent orientation of the ordinary and extraordinary axes in the transverse plane [69, 70]. The structure of such axes' distribution is characterized by a number, known as the topological charge q . This device is mainly used in optics for the generation of structured light, which are, inhomogeneous light beams containing particular phase or polarization singularities, with interesting properties and applications in microscopy, particle manipulation, quantum information processing, among others [71–73].

Recently, two exciting technologies are experiencing significant progress: terahertz devices and 3D printers. Terahertz radiation is now used in industrial quality control [74], characterization of materials [75] and free-space communications [76]. A 3D printer has become an apparatus able to rapidly fabricate complicated geometrical objects at affordable prices. Fortunately, some polymers, that can be used with a 3D printer, are transparent in the THz band, which allows the fabrication of THz devices, such as lenses [77, 78],

waveguides [79, 80], and gratings [81, 82] and form birefringent wave-plates [83]. Furthermore, a THz vortex generation using 3D printed devices was demonstrated [84]. The usual way to generate this THz vectorial beams is using a segmented quartz plate [85].

5.1 Mathematical description

Consider a q -plate having a homogeneous phase retardation of π (half-wave) for light traveling in the longitudinal z direction. The plate has a transversely inhomogeneous birefringent axes distribution $\mathbf{o}(x, y)$, lying in the xy plane. Consider that $\alpha(x, y)$ is the angle between $\mathbf{o}(x, y)$ and the x axis. Let $\alpha(x, y)$ be given by the following equation

$$\alpha(r, \phi) = q\phi + \alpha_0, \quad (5.1)$$

where r, ϕ are the polar coordinates in the transverse plane, q and α_0 are constants. In order to visualize the effect of this q -plate, consider a horizontally polarized plane wave $\mathbf{E}_{in} = E_0\hat{\mathbf{x}}$ impinging on the q -plate at normal incidence. The Jones matrix of a q -plate is given by

$$\mathbf{H} = \begin{bmatrix} \cos 2\alpha & \sin 2\alpha \\ \sin 2\alpha & -\cos 2\alpha \end{bmatrix}, \quad (5.2)$$

for the basis of linear polarizations $(\hat{\mathbf{x}}, \hat{\mathbf{y}})$. In this basis, the q -plate with $q = 1/2$ and $\alpha_0 = 0$ transforms the incident beam into

$$\mathbf{E}_{out} = \begin{bmatrix} \cos \phi & \sin \phi \\ \sin \phi & -\cos \phi \end{bmatrix} \begin{bmatrix} E_0 \\ 0 \end{bmatrix} = E_0 \begin{bmatrix} \cos \phi \\ \sin \phi \end{bmatrix}, \quad (5.3)$$

which can be expressed in the form $\mathbf{E}_{out} = E_0 \cos \phi \hat{\mathbf{x}} + E_0 \sin \phi \hat{\mathbf{y}} = E_0 \hat{\mathbf{r}}$. Therefore, the outgoing wave shows a radial polarization distribution. It is straightforward to show that if the incident field is vertically polarized, the outgoing wave will show an azimuthal polarization mode $\mathbf{E}_{out} = E_0 \hat{\phi}$.

Beams with radial or azimuthal polarization distribution are of interest in singular optics and find applications in tight focusing and waveguide coupling. Their intensity pattern has characteristic annular shape, showing a central singularity in the electric field distribution.

The use of 3D-printing opens the possibility to create complex terahertz quasi-optical components that incorporate form-induced-birefringence [86]. Most q -plates reported to date divide the area of the plate in a finite number of sections. In each section a birefringent material or structure is placed at a given orientation, this way the polarization of the beam propagating through the q -plate is modified in each section, producing an electromagnetic mode which has a polarization that is a discretized version of the desired mode. In our case, the possibility of introducing form-birefringence on the 3D-printed component, allows us to continuously vary the direction of the birefringence. The so-called streamlines of the q -plate define the local direction of the slow or fast axis (there is only a global phase difference between the resulting beams of both cases).

For a q -plate with $q = 1/2$ and $\alpha_0 = 0$ the optical axis α is given by $\alpha = \phi/2$ where ϕ is the polar angle in cylindrical coordinates. We can define

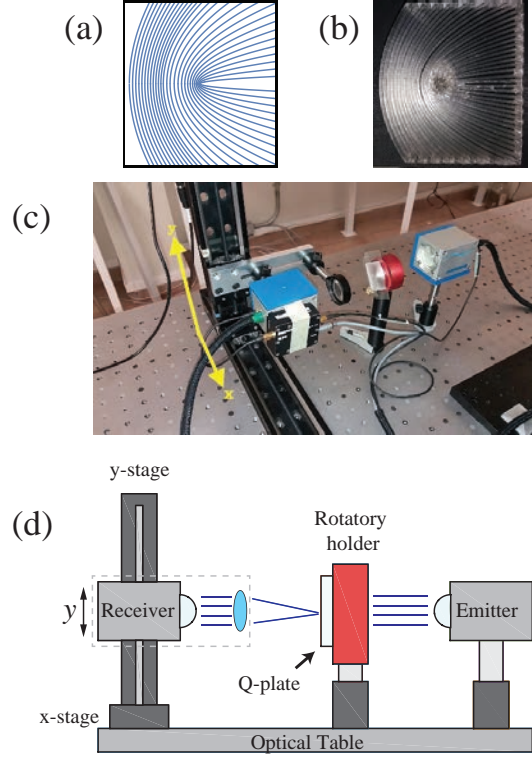


Figure 5.1: The top row shows the fabricated q -plate, b), along with the theoretical pattern, a). The plate has transverse dimensions $40 \times 40 \text{ mm}^2$ with a thickness of 5 mm. Figures c) and d) show the actual experimental setup. The operating frequency is 150 GHz (0.15 THz). The scanning system has a step size of 1 mm.

a unit vector field describing the optical axis distribution as

$$\mathbf{u} = \cos(\phi/2)\hat{\mathbf{x}} + \sin(\phi/2)\hat{\mathbf{y}}. \quad (5.4)$$

In order to obtain the streamlines generated by this vector field, we have to solve the differential equation $y'(x) = u_x/u_y$, where (u_x, u_y) are the Cartesian components of \mathbf{u} . Using Eq. (5.4) we have

$$\frac{dy}{dx} = \frac{u_y}{u_x} = \frac{\sin(\phi/2)}{\cos(\phi/2)} = \tan(\phi/2). \quad (5.5)$$

We use the identity $\tan(\phi/2) = \sin \phi / (1 + \cos \phi)$ and change to Cartesian coordinates with $\sin \phi = y / (x^2 + y^2)^{1/2}$ and $\cos \phi = x / (x^2 + y^2)^{1/2}$. The resulting differential equation is

$$\frac{dy}{dx} = \frac{y}{\sqrt{x^2 + y^2} + x}, \quad (5.6)$$

which has solutions of the form

$$y(x) = \pm e^{C/2} \sqrt{e^C + 2x}, \quad (5.7)$$

where C is a real constant that characterizes a particular streamline. With the initial condition $y(0) = y_0$, we obtain

$$y(x) = \pm \sqrt{y_0} \sqrt{y_0 + 2x}. \quad (5.8)$$

Equation (5.8) is the one that we use for the fabrication of the q -plate. The resulting pattern is shown in Fig. 5.1 (a).

5.2 Fabrication and results

We use a fused deposition modeling (FDM) Prusa i3 3D printer for the fabrication of the q -plate. The 3D printer heats the plastic and deposits it layer-by-layer with a thickness of about $400\mu m$. The transverse resolution is determined by the diameter of the nozzle, which in our case has a diameter of $400\mu m$. Structures with discontinuous features are difficult to print with reasonable quality, because it implies stopping and starting the flow of

plastic along the printing trajectories which, in turn, introduces imperfection in the printed object. Therefore, we decided to print the optical axis streamlines as described in the previous section. In this way the structure could be printed with a continuous injection of material producing a soft and continuous trajectory.

For the generation of cylindrical vector beams, we fabricated the q -plate with $q = 1/2$, which is shown in Fig. 6.3b. In order to describe the interaction between the device and the radiation we used the effective medium theory, given that the wavelength of the THz radiation (150 GHz = 2 mm) is larger than the q -plate features (400 μm).

In a strip line structure (as locally in the q -plate), the effective refractive index of the structure for radiation with polarization parallel and perpendicular to the strip lines is given by [68]

$$n_e^2 = n_{\parallel}^2 + \frac{1}{3} \left[\frac{\Lambda}{\lambda} \pi f_1 f_2 (n_1^2 - n_2^2) \right]^2, \quad (5.9)$$

$$n_o^2 = n_{\perp}^2 + \left[\frac{\Lambda}{\lambda} \pi f_1 f_2 \left(\frac{1}{n_1^2} - \frac{1}{n_2^2} \right) n_{\parallel} n_{\perp}^3 \right]^2, \quad (5.10)$$

respectively, where Λ is the period of the strip lines, λ is the wavelength, f_1 and f_2 the volumetric fraction of the constituent materials and n_1 and n_2 are the refractive indices of the polymer, bendlay in this case ($n_1 = 1.5$ measured by transmission TDS), and air ($n_2 = 1$), respectively, where

$$n_{\parallel}^2 = f_1 n_1^2 + f_2 n_2^2, \quad (5.11)$$

$$n_{\perp}^2 = \left(\frac{f_1}{n_1^2} + \frac{f_2}{n_2^2} \right)^{-1}. \quad (5.12)$$

Based on these equations it is possible to make different kinds of birefringent devices, for example, half-waveplates. According to the theory we need a continuous orientation variation of a half-waveplate in order to produce a continuous q -plate. Every local section shown in Fig. 5.1 (a) is a half-waveplate with a different orientation angle, necessary for the generation of the cylindrical vector beam. The printed device is shown in Fig. 5.1 (b). The thickness of the structure is calculated using the birefringence of the structure. In particular, the structure proposed in this work had a birefringence of 0.1. So the thickness of the structure is 5 mm for a half-waveplate at 150 GHz. In order to measure the polarization distribution of the beam after propagation through the q -plate, we used a terahertz time-domain imaging system. A schematic of the experimental setup is shown in Fig. 5.1 (d)

We used the same spectrometer as in previous sections. In addition the receiver was mounted on two translational stages forming an optical system that collects the radiation at a given point on the q -plate that can be raster scanned across its surface. The photoconductive detector is only sensitive to the electric field in one linear polarization direction, therefore the detector had to be rotated by 90° in order to obtain the two components of the terahertz electric field. A terahertz waveform is measured on a 40 mm by 40 mm mesh with 1 mm steps in order to obtain the full position-dependent electric field of the beam after propagation through the q -plate.

Figure 5.2 shows the experimental measurements. In order to produce a radially polarized beam, the incident polarization should be parallel to the

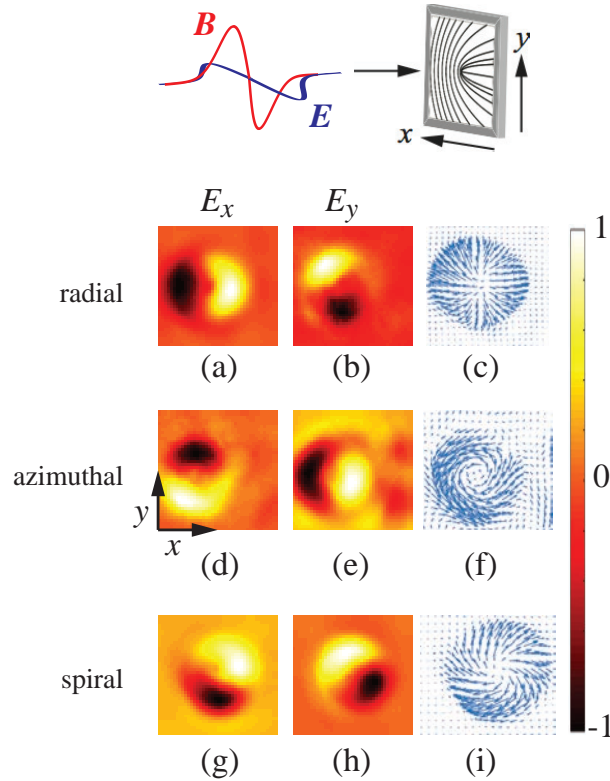


Figure 5.2: Transverse amplitude measurements with THz-TDI. A terahertz pulse with homogeneous linear polarization propagates through a q -plate oriented as shown in the top row. Figures (a) and (b) show the electric field components E_x and E_y , respectively, when the incident field is oriented along x . It produces a radial polarization distribution, which is shown in (c). Figures (d), (e) and (f) show the same measurements when the incident electric field is polarized along y , which produces a vector field with azimuthal polarization. In general, if the polarization of the incident field forms an arbitrary angle with respect to x , the outgoing field will have spiral polarization distribution, which is shown in Figs. (g), (h), (i), where we used a field with polarization oriented at 45° .

singular straight line of the q -plate. The experiment is set-up as shown in the top row of Fig. 5.2. Hence, a horizontally polarized beam is transformed into a “radially polarized” beam and a vertically polarized beam becomes an azimuthal vector beam. The Figs. 5.2 (a) and (b) show the 150 GHz terahertz electric field E_x and E_y components respectively when presented in

the form of a vector field [Fig. 5.2 (c)], it is easy to see that the electromagnetic mode shows radial polarization distribution. The slight asymmetry observed in Figs. 5.2 (b) is caused by minor mismatch of the optical axis of the beam and that of the q -plate. From Eq. (5.3) we see that $E_x \propto \cos \phi$ and $E_y \propto \sin \phi$, which shows good agreement with the experimental results. Analogous measurements were performed after rotating the q -plate 90° . The E_x and E_y components for these measurements are shown in Figs. 6.4(d) and (e). The vector field formed in this case, presented in Fig. 5.2 (f), shows an azimuthal distribution. Given that $\lambda = 2 \text{ mm}$ (150 GHz), the q -plate structure is an effective medium since the structure features are significantly smaller ($400 \mu\text{m}$), therefore the wavefront of the cylindrical beam should not be affected by scattering.

Radially and azimuthally “polarized” beams are particular cases of a more general class of vector beams, the “spirally polarized” ones [87]. If the incident electric field forms different angle with respect to the singular line of the q -plate, the field will emerge having spiral polarization distribution. Figures 5.2 (g), (h) and (i) show the resulting spiral polarization distribution when the incident electric field is oriented 45° with respect to x .

Chapter 6

Artificial dielectric

stepped-refractive-index lens

In order to expand the applications for terahertz (THz) radiation [88], the generation of new devices and components for the manipulation of THz radiation are necessary. There has been an effort to fabricate lenses using 3D printing techniques [77, 78, 82, 89], compressing powders [90], using ring-resonators-based metamaterials [91–94] and more recently, using artificial dielectrics made of parallel plate waveguides (PPWGs) [95–99]. Artificial dielectrics are man-made media that mimic the properties of naturally occurring dielectric media, or even manifest properties that cannot generally occur in nature. For example, the well-known dielectric property, the refractive index, which usually has a value greater than unity, can have a value less than unity in an artificial dielectric. In this section we designed and experimentally proved that a modulation of the refractive index of an artificial dielectric made of PPWGs is possible by controlling the plate spacing from

1.5 mm at the center of the device to 0.8 mm in the outer periphery of the device, where every PPWG has the same propagation length, resulting in a flat lens. The clear aperture of the device is large enough to neglect edge effects and to ensure that only the TE_1 mode is dominantly excited [100]. We demonstrate that this artificial dielectric stepped-index lens is capable of focusing a 10 mm diameter beam into line focus of less than 4 mm at the design frequency of 0.18 THz.

6.1 Design and Fabrication

A simplified schematic diagram of the artificial dielectric device is shown in Figs. 6.1 (a) and (b). It consists of an assembly of non-uniformly spaced identical parallel plates made of $100\ \mu\text{m}$ thick titanium with spacings from 0.8 mm to 1.5 mm, which gives a ratio between 8 and 15 of the spacing compared to the thickness. The plates were fabricated by chemical etching in order to prevent any burring. We used three types of spacers with different thickness, 0.3 mm, 0.5 mm and 1.0 mm. Using linear combinations of these three thicknesses, we realized plate spacings varying from 0.8 mm to 1.5 mm in steps of 0.1 mm. Fig. 6.1 (b) shows a front view of the device, where the variation of the spacing between plates is illustrated. The plot in Fig. 6.1 (c) is the theoretical variation of the effective refractive index as a function of the plate spacing for different frequencies [101, 102]. This plot shows that the index is highly dependent on the plate spacing. The effective-refractive-index function of the device is given by

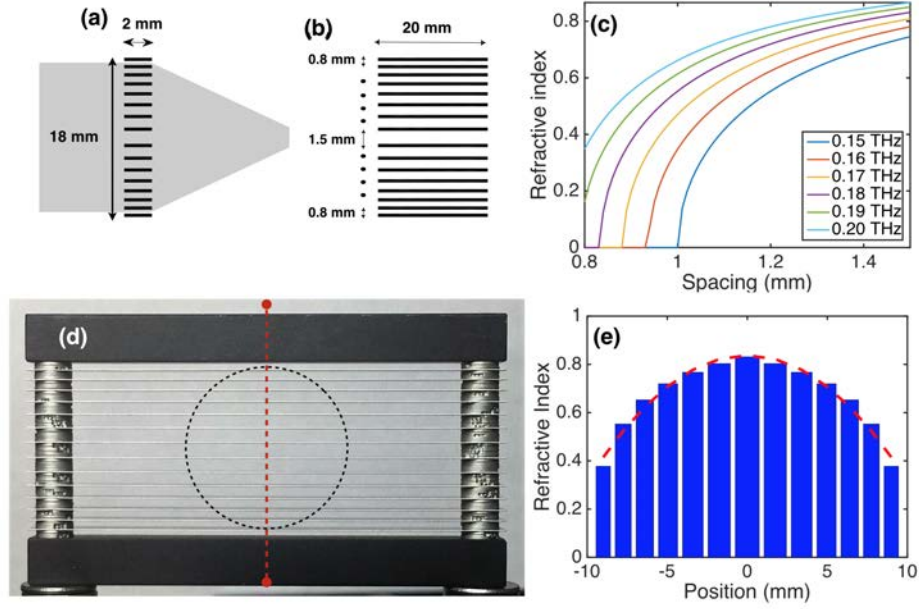


Figure 6.1: Schematic diagram of the device. (a) lateral view, (b) front view (the aspect ratio of the device was exaggerated for clarity). (c) refractive index of a typical PPWG operating in the TE_1 mode as function of the plate spacing for frequencies from 0.15 THz to 0.20 THz (d) Photograph of the fabricated device. The dotted circle denotes the incident beam. (e) Index profile of the structure at 0.18 THz along the red dotted line in (d). In (e) the red dashed line is a parabolic fit to the refractive index profile.

$$n = \sqrt{1 - \frac{c^2}{4h^2f^2}}, \quad (6.1)$$

where f is the frequency, c is the speed of light in vacuum and h is the plate spacing. Fig. 6.1 (d) shows a photograph of the fabricated device, looking on axis, which illustrates a clear aperture of 20 mm by 18 mm. Fig. 6.1 (e) shows the refractive-index profile of the structure at 0.18 THz along the red dotted line in (d). In the same figure, we plot a parabolic fit in order to emphasize the quadratic variation of the refractive index profile .

The operating principle of our device relies on the propagation of the TE_1

mode in every individual PPWG constituting the artificial dielectric structure. The refractive index of each PPWG is a function of the plate spacing as shown in Fig. 6.1 (c) . When the spacing between the plates decreases, the refractive index also decreases, for a given frequency.

In order to verify the operation of this device, we used a commercial finite-element method (FEM) software, COMSOL Multiphysics, to perform numerical simulations for frequencies from 0.17 THz to 0.20 THz in steps of 0.01 THz. The metal plates of the device are considered as perfect electric conductors (PECs). The device is illuminated by a collimated Gaussian beam with an amplitude of 1 V/m. In order to ensure the accuracy, the length scale of the mesh is set to be less than or equal to $\lambda/8$ throughout the simulation domain, where λ is the wavelength of the incident radiation. These results are shown in Fig. 6.2. The focusing of the THz radiation by the device is clearly observed in Fig 6.2 (a) and (b). Fig 6.2 (a) and (b) show the instantaneous electric field and the normalized intensity respectively, at a frequency of 0.18 THz. The input electric-field vector is parallel to the plates to excite the TE_1 mode. In Fig 6.2 (a) the formation of the wavefront curvature inside the structure is clearly seen as the wave propagates, which causes to generate a focus. In Fig 6.2 (b) the intensity shows a strong focus approximately 10 mm after the front face of the lens. In Fig 6.2 (c) we present simulation results for 0.17 - 0.21 THz in the in order to find the maximum electric-field amplitude. This figure shows that the strongest focus is at 0.18 THz (the design frequency). These simulation results predict a focus with an approximately 2 mm beam waist. The focal length clearly exhibits chromatic aberration, shifting to larger distances for larger frequencies. In

Fig. 6.2 (d) the predicted wavefront position after propagating 4.3 ps is shown in red lines superimposed on the simulation. The position of the wavefront was found theoretically using

$$E(t) = e^{i\omega t}, \quad (6.2)$$

where $\omega = ck_0n$, where c is the speed of light in vacuum, k_0 the wavenumber in vacuum, n the refractive index of the device as given in Eq. (6.1), and t the time. Fig. 6.2 (d) shows excellent agreement between the simulation and the analytical result; the wavefront engineering due to the particular index profile of the structure.

6.2 Experimental characterization

The experimental characterization was carried out using a fiber-coupled commercial time-domain spectrometer which generates and detects radiation in the THz band. The schematic of the experimental setup is illustrated in Fig 6.3. The input beam to the lens was formed to a 1/e-amplitude diameter of 10 mm as used in the numerical simulations. For the detection we used an effective aperture of 0.5 mm diameter placed in front of the receiver (silicon lens) in order to improve the spatial resolution. The data were collected by scanning the aperture-integrated receiver along a 20 mm line with steps of 0.5 mm in the direction transverse to the input beam axis, as shown in Fig 6.3. We recorded the broadband pulses passing through the device which were subsequently Fourier transformed in order to extract their spectral content. In Fig 6.4 we show the measured beam profiles for 0.15 THz, 0.18 THz

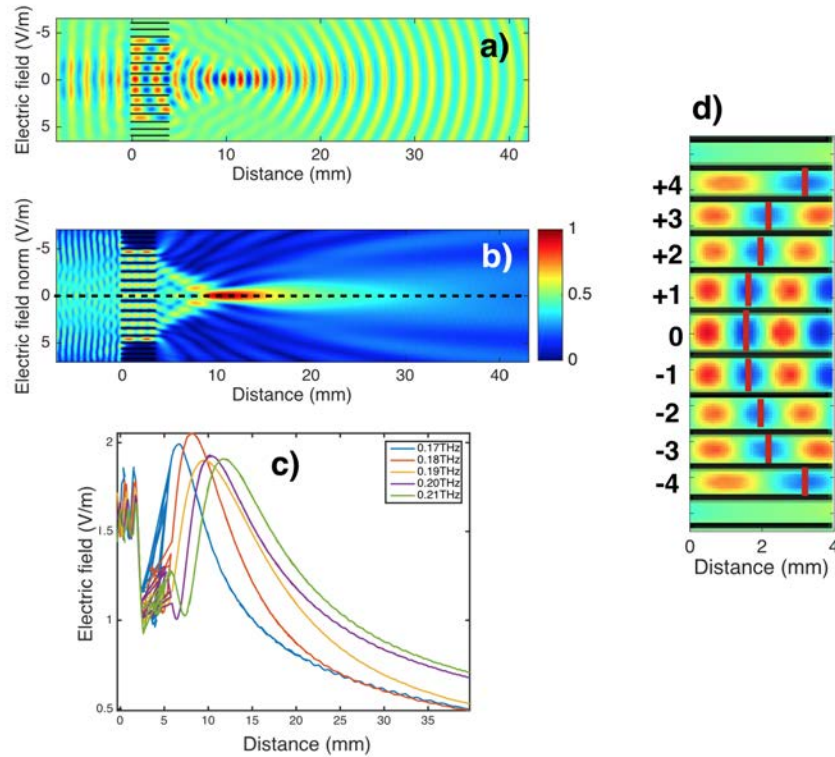


Figure 6.2: Numerical simulation results. (a) Instantaneous electric field and (b) normalized electric field at 0.18 THz. (c) longitudinal cross-section along the dotted line in Fig (b) for the same simulation but for frequencies from 0.17 THz to 0.21 THz in steps of 0.01 THz. In (a) and (b) the focus is clearly identified at approximately 10 mm from the front face of the lens. This distance is confirmed in (c) where the maximum amplitude is at approximately 10 mm for $f = 0.18$ THz. Figure (d) shows the predicted wavefront position after 4.3 ps (red lines) using eq. (6.2).

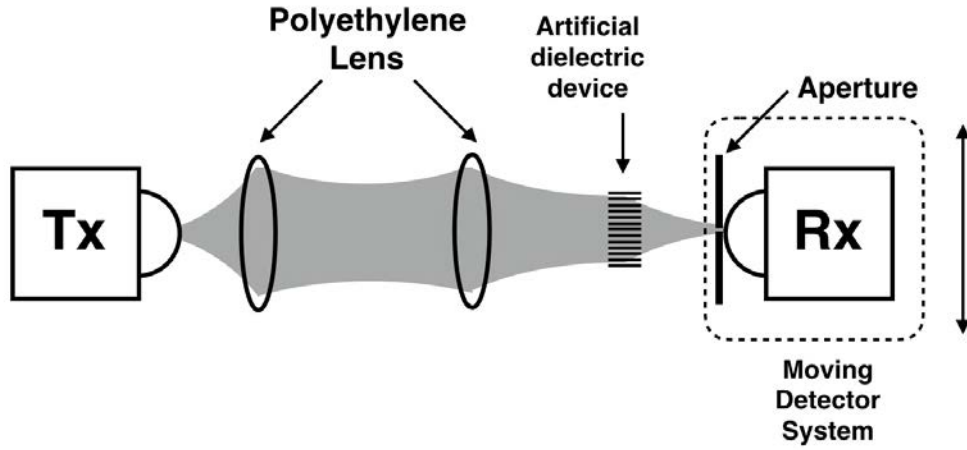


Figure 6.3: Schematic of the experimental setup for the experimental characterization of the focusing properties for the artificial dielectric stepped-index device.

and 0.20 THz.

From these results we see that the maximum amplitude is achieved at 0.18 THz, in agreement with the simulations. The major differences between the simulations and the experimental results are in the focal distance and the size of the focus. They were respectively, 10 mm and 2 mm for the simulation and 18 mm and 3.34 mm for the experiment. These discrepancies are most likely due to the imperfections in the device; in other words, the plates were not perfectly flat. In addition, secondary lobes are seen on either side of the main lobe. The secondary lobes are due the truncation of the input beam, which becomes more severe as the frequency goes down, due to the TE_1 cutoff. This can be understood from Fig 6.2 (a). For example, at 0.18 THz the clear aperture is determined by the location of PPWGs with spacing of 0.9 mm, since smaller spacings are below cutoff at this frequency. As a result, the beam is clipped for plate spacings smaller than 0.9 mm, causing

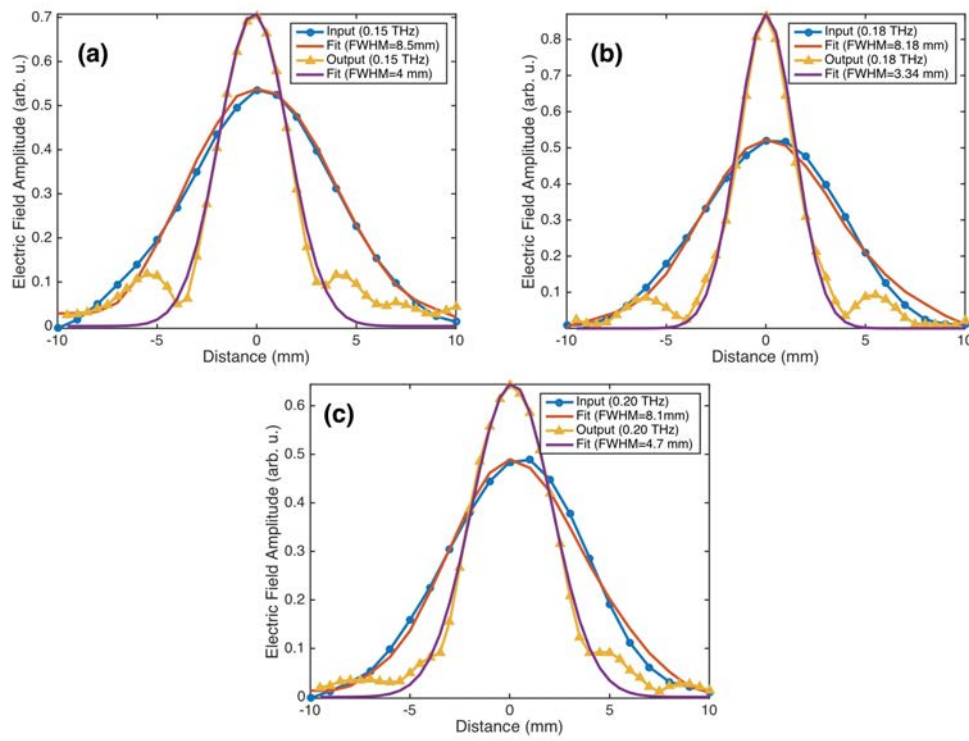


Figure 6.4: Cross sectional profile for the input and output beams for a) 0.15 THz, b) 0.18 THz and c) 0.20 THz. The data were recorded at 18 mm from the front surface of the device. In the same figures Gaussian fits are shown.

this “ringing” effect in the focal plane.

In order to understand the device further, we also carried out an analytical examination of the device. In the model, we used the Rayleigh-Sommerfeld Integral given by [103, 104].

$$U_2(x, y) = \frac{z}{j\lambda} \iint_{\Sigma} U_1(\xi, \eta) \frac{\exp(jkr_{12})}{r_{12}^2} d\xi d\eta, \quad (6.3)$$

where U_2 is the electric field at the observation position, λ the wavelength, z the perpendicular distance from the incident plane to the observation plane, U_1 the electric field at the incident plane, $k = k_0 n$ the wavenumber in vacuum multiplied by the fitted refractive index of the device given by the red dashed curve in Fig 6.1 (e) and r_{12} the distance from the incident plane to a point on the observation plane.

In Fig 6.5 we compare the experimental beam profile with our numerical and theoretical result at 0.18 THz. This comparison shows very good agreement between the analytical and simulation results of the size of the focus. The slightly larger experimental result is due to device imperfections as noted earlier.

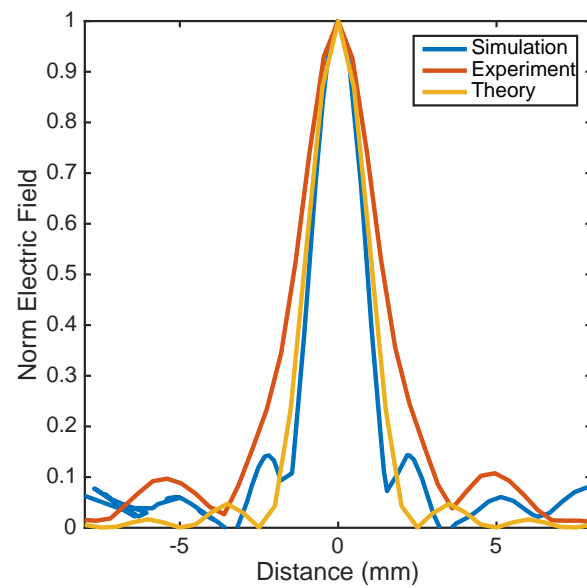


Figure 6.5: Comparison between cross section of the beam for the numerical simulation (blue line), experimental result (red line) and theoretical result (yellow line). It is observed that the beam waist for the experimental result is larger than the theoretical and the simulation one. This is most likely due the imperfections on the device.

Chapter 7

Conclusion

In this thesis we show four new devices for the manipulation of THz radiation, three of them were 3D printed, GRIN lens, polarization splitter and q-plate and the last one is a novel stepped-refractive-index lens fabricated by artificial dielectric.

In the case of the 3D printed GRIN lens our measurements demonstrate that these devices operate within the diffraction limit for the frequencies below 800 GHz ($\lambda > 375 \mu m$). We also investigate the chromatic aberration, given that the lenses presented are based on an effective medium combining air and polystyrene in order to produce refractive index gradient, which at its time produce variations for the effective refractive index experienced by each frequency. This new kind of lenses show some advantages compared with the conventional spherical lenses, given that they are thin and flat on both faces and their focal distances can be tailored by controlling the refractive index gradient, in addition, they are easily to fabricate, and a very low cost.

Furthermore, we used the form birefringence effect in order to build the

first 3D printed THz polarization splitter, similar to a Wollaston prism. The structure consist in a 2 cm side cube made of Bendlay ($n=1.53$). One half of the device consists of a birefringent triangular structure and the other half is a solid prism. The device operates very well for frequencies below 400 GHz. A polarization splitter such as this one is useful for the construction of terahertz photonic systems and might be applied to multiplexing and demultiplexing signals for terahertz telecommunications. In addition, the mass production of this component is viable

We also explored the vectorial beam area where unconventional polarization modes of light are studied. In order to generate this exotic polarization modes we have presented a simple fabrication method of a q -plate for the generation of terahertz cylindrical vector beams. The q -plate was fabricated with a commercial 3D printer. The cylindrical beams were measured using time domain imaging. This device can be used to efficiently couple terahertz radiation into waveguides, where segmented waveplates are used to generate radially polarized beams. Furthermore, other q -plates can be fabricated for the generation of complex-structured vector beams in order to study physical phenomena of interest in singular optics, such as orbital angular momentum and polarization topologies

In addition we present, to the best of our kwnoledge, the first experimental evidence of an artificial dielectric stepped-refractive-index lens for the terahertz regime. The device was build using parallel plate waveguides technology. Using a multi-stack structure and varying the separation of the stack, a stepped-refractive -index profile was produced. In particular, by linearly varyng the spacing of the plates from 0.8 mm at the outer part of the

structure to 1.5 mm in the center of the device in steps of 0.1 mm a gradient in the refractive index was produced. We experimentally demonstrated that this novel device is capable of focusing a 10 mm diameter beam to a size of 4 mm at 0.18 THz. The refractive behavior of this device is achieved via the spatial index variation and not via the surface geometry, making this a flat lens. This device, made of equal size metallic plates, has advantages in comparison to other artificial dielectric lenses in the sense the faces of the device are flat, which can be easier to assemble, produce and incorporated to some optical systems. This kind of frequency dependent devices can be used for a multispectral analysis and even for telecommunications applications.

All these four devices can be used in communications for the next generation of terahertz equipment. Furthermore we confirm that 3D printing is promising technique for prototyping and fabricating relatively sophisticated quasi-optical devices, currently unavailable, for terahertz frequencies.

Bibliography

- [1] Y.S. Lee. *Principles of Terahertz Science and Technology*. Springer, 2010.
- [2] Simon M Sze and Kwok K Ng. *Physics of semiconductor devices*. John Wiley & Sons, 2006.
- [3] D. H. Auston and M. C. Nuss. *Electrooptic generation and detection of femtosecond electrical transients*. IEEE J. Quantum Electron., 24:184–197, 1988.
- [4] M Bass, P A Franken, J F Ward, and G Weinreich. *Optical rectification*. Phys. Rev. Lett., 9:446–448, 1962.
- [5] Orazio Svelto and David C Hanna. *Principles of lasers*. 1998.
- [6] Timothy D Dorney, Richard G Baraniuk, and Daniel M Mittleman. *Material parameter estimation with terahertz time-domain spectroscopy*. JOSA A, 18(7):1562–1571, 2001.
- [7] Lionel Duvillaret, Frédéric Garet, J-F Roux, and J-L Coutaz. *Analytical modeling and optimization of terahertz time-domain spectroscopy experiments, using photoswitches as antennas*. Selected Topics in Quantum Electronics, IEEE Journal of, 7(4):615–623, 2001.
- [8] KA McIntosh, KB Nichols, S Verghese, and ER Brown. *Investigation of ultrashort photocarrier relaxation times in low-temperature-grown gaas*. Applied physics letters, 70(3):354–356, 1997.
- [9] B Sartorius, H Roehle, H Künzel, J Böttcher, M Schlak, D Stanze, H Venghaus, and M Schell. *All-fiber terahertz time-domain spectrometer operating at 1.5 μm telecom wavelengths*. Optics Express, 16(13):9565–9570, 2008.
- [10] John David Jackson and John D Jackson. *Classical electrodynamics*, volume 3. Wiley New York etc., 1962.

-
- [11] P. R. Smith, D. H. Auston, and M. C. Nuss. *Subpicosecond photoconducting dipole antennas*. IEEE J. Quantum Electron., 24:255–260, 1988.
- [12] P. U. Jepsen, R. H. Jacobsen, and S. R. Keiding. *Generation and detection of terahertz pulses from biased semiconductor antennas*. J. Opt. Soc. Am. B, 13:2424–2436, 1996.
- [13] John F Federici, Brian Schulkin, Feng Huang, Dale Gary, Robert Barat, Filipe Oliveira, and David Zimdars. *Thz imaging and sensing for security applications-explosives, weapons and drugs*. Semiconductor Science and Technology, 20(7):S266, 2005.
- [14] Dwight L Woolard, William R Loerop, and Michael Shur. *Terahertz sensing technology: emerging scientific applications & novel device concepts*, volume 2. World scientific, 2003.
- [15] Nick C. J. van der Valk, Willemine A. M. van der Marel, and Paul C. M. Planken. *Terahertz polarization imaging*. Opt. Lett., 30(20):2802–2804, 2005.
- [16] P Uhd Jepsen, David G Cooke, and Martin Koch. *Terahertz spectroscopy and imaging—modern techniques and applications*. Laser & Photonics Reviews, 5(1):124–166, 2011.
- [17] J. M. Chamberlain. *Where optics meets electronics: recent progress in decreasing the terahertz gap*. Phil. Trans. R. Soc. A, 362:199–211, 2004.
- [18] Benjamin Born, Seung Joong Kim, Simon Ebbinghaus, Martin Gruebele, and Martina Havenith. *The terahertz dance of water with the proteins: the effect of protein flexibility on the dynamical hydration shell of ubiquitin*. Faraday discussions, 141:161–173, 2009.
- [19] Ernest V Loewenstein, Donald R Smith, and Robert L Morgan. *Optical constants of far infrared materials. 2: Crystalline solids*. Applied optics, 12(2):398–406, 1973.
- [20] D. F. Liu and J. Y. Qin. *Carrier dynamics of terahertz emission from low-temperaturegrown GaAs*. Appl. Opt., 42:3678–3683, 2003.
- [21] Peter Uhd Jepsen, Hannes Merbold, et al. *Investigation of aqueous alcohol and sugar solutions with reflection terahertz time-domain spectroscopy*. Optics Express, 15(22):14717–14737, 2007.

- [22] Yoshiaki Yomogida, Yuki Sato, Ryusuke Nozaki, Tomobumi Mishina, and Junichiro Nakahara. *Comparative study of boson peak in normal and secondary alcohols with terahertz time-domain spectroscopy*. Physica B: Condensed Matter, 405(9):2208–2212, 2010.
- [23] SR Keiding. *Dipole correlation functions in liquid benzenes measured with terahertz time domain spectroscopy*. The Journal of Physical Chemistry A, 101(29):5250–5254, 1997.
- [24] Partha Dutta and Keisuke Tominaga. *Dependence of low frequency spectra on solute and solvent in solutions studied by terahertz time-domain spectroscopy*. Molecular Physics, 107(18):1845–1854, 2009.
- [25] Asako Oka and Keisuke Tominaga. *Terahertz spectroscopy of polar solute molecules in non-polar solvents*. Journal of non-crystalline solids, 352(42):4606–4609, 2006.
- [26] Youngseon Shim and Hyung J Kim. *Dielectric relaxation, ion conductivity, solvent rotation, and solvation dynamics in a room-temperature ionic liquid*. The Journal of Physical Chemistry B, 112(35):11028–11038, 2008.
- [27] Mattijs Koeberg, Chien-Ching Wu, Doseok Kim, and Mischa Bonn. *Thz dielectric relaxation of ionic liquid: water mixtures*. Chemical physics letters, 439(1):60–64, 2007.
- [28] H. Nemeč, A. Pashkin, P. Kuzel, M. Khazan, S. Schnull, and I. Wilke. *Carrier dynamics in low-temperature grown GaAs studied by terahertz emission spectroscopy*. J. Appl. Phys., 90:1303–1306, 2001.
- [29] SC Corzo-Garcia, AI Hernandez-Serrano, E Castro-Camus, and O Mitrofanov. *Monte carlo simulation of near-field terahertz emission from semiconductors*. Physical Review B, 94(4):045301, 2016.
- [30] B. G. Danly, S. G. Evangelides, R. J. Temkin, and B. Lax. *A tunable far infrared-laser*. IEEE J. Quantum Electron., 20:834–837, 1984.
- [31] E Castro-Camus, M Palomar, and AA Covarrubias. *Leaf water dynamics of arabidopsis thaliana monitored in-vivo using terahertz time-domain spectroscopy*. Scientific reports, 3, 2013.
- [32] Jun-ichi Nishizawa, Tetsuo Sasaki, Ken Suto, Tetsuya Yamada, Tadao Tanabe, Takenori Tanno, Takashi Sawai, and Yasuhiro Miura. *Thz imaging of nucleobases and cancerous tissue using a gap thz-wave generator*. Optics communications, 244(1):469–474, 2005.

- [33] E Pickwell, BE Cole, AJ Fitzgerald, M Pepper, and VP Wallace. *In vivo study of human skin using pulsed terahertz radiation*. *Physics in Medicine and Biology*, 49(9):1595, 2004.
- [34] Anthony J Fitzgerald, Vincent P Wallace, Mercedes Jimenez-Linan, Lynda Bobrow, Richard J Pye, Anand D Purushotham, and Donald D Arnone. *Terahertz pulsed imaging of human breast tumors*. *Radiology-Radiological Society of North America*, 239(2):533–540, 2006.
- [35] Shengyang Huang, Philip C Ashworth, Kanis W Kan, Yang Chen, Vincent P Wallace, Yuan-ting Zhang, and Emma Pickwell-MacPherson. *Improved sample characterization in terahertz reflection imaging and spectroscopy*. *Optics express*, 17(5):3848–3854, 2009.
- [36] E Pickwell and VP Wallace. *Biomedical applications of terahertz technology*. *Journal of Physics D: Applied Physics*, 39(17):R301, 2006.
- [37] Wenhui Fan. *Broadband terahertz spectroscopy*. *Chinese Optics Letters*, 9(11):110008, 2011.
- [38] AM Gomez-Sepulveda, AI Hernandez-Serrano, R Radpour, CL Koch-Dandolo, SC Rojas-Landeros, LF Ascencio-Rojas, Alvaro Zarate, Gerardo Hernandez, RC Gonzalez-Tirado, M Insaurralde-Caballero, et al. *History of mexican easel paintings from an altarpiece revealed by non-invasive terahertz time-domain imaging*. *Journal of Infrared, Millimeter, and Terahertz Waves*, 38(4):403–412, 2017.
- [39] CL Koch Dandolo, AM Gomez-Sepulveda, AI Hernandez-Serrano, and E Castro-Camus. *Examination of painting on metal support by terahertz time-domain imaging*. *Journal of Infrared, Millimeter, and Terahertz Waves*, 38(10):1278–1287, 2017.
- [40] Aurélie JL Adam, Paul Planken, Sabrina Meloni, and Joris Dik. *Terahertz imaging of hidden paint layers on canvas*. *Optics Express*, 17(5):3407–3416, 2009.
- [41] JB Jackson, M Mourou, JF Whitaker, IN Duling III, SL Williamson, M Menu, and GA Mourou. *Terahertz imaging for non-destructive evaluation of mural paintings*. *Optics Communications*, 281(4):527–532, 2008.
- [42] Kaori Fukunaga and Marcello Picollo. *Characterisation of works of art*. In *Terahertz Spectroscopy and Imaging*, pages 521–538. Springer, 2013.

-
- [43] Ian Gibson, David W Rosen, Brent Stucker, et al. *Additive manufacturing technologies*, volume 238. Springer, 2010.
- [44] Bharat Bhushan and Matt Caspers. *An overview of additive manufacturing (3d printing) for microfabrication*. *Microsystem Technologies*, 23(4):1117–1124, 2017.
- [45] Salih Ergün and Selçuk Sönmez. *Terahertz technology for military applications*. *Journal of Military and Information Science*, 3(1):13–16, 2015.
- [46] Rayko Ivanov Stantchev, Baoqing Sun, Sam M Hornett, Peter A Hobson, Graham M Gibson, Miles J Padgett, and Euan Hendry. *Noninvasive, near-field terahertz imaging of hidden objects using a single-pixel detector*. *Science Advances*, 2(6):e1600190, 2016.
- [47] AI Hernandez-Serrano, SC Corzo-Garcia, E Garcia-Sanchez, M Alfaro, and E Castro-Camus. *Quality control of leather by terahertz time-domain spectroscopy*. *Applied optics*, 53(33):7872–7876, 2014.
- [48] M Stecher, C Jördens, N Krumbholz, C Jansen, M Scheller, R Wilk, O Peters, B Scherger, B Ewers, and M Koch. *Towards industrial inspection with thz systems*. In *Ultrashort Pulse Laser Technology*, pages 311–335. Springer, 2016.
- [49] M Theuer, R Beigang, and D Grischkowsky. *Highly sensitive terahertz measurement of layer thickness using a two-cylinder waveguide sensor*. *Applied Physics Letters*, 97(7):071106, 2010.
- [50] Kaori Fukunaga. *Thz technology applied to cultural heritage in practice*, 2016.
- [51] Corinna L Koch-Dandolo, Troels Filtenborg, Kaori Fukunaga, Jacob Skou-Hansen, and Peter Uhd Jepsen. *Reflection terahertz time-domain imaging for analysis of an 18th century neoclassical easel painting*. *Applied optics*, 54(16):5123–5129, 2015.
- [52] Wanzheng Hu, S Catalano, M Gibert, J-M Triscone, and Andrea Cavalleri. *Broadband terahertz spectroscopy of the insulator-metal transition driven by coherent lattice deformation at the smni o 3/laal o 3 interface*. *Physical Review B*, 93(16):161107, 2016.
- [53] Naoto Oshima, Kazuhide Hashimoto, Daisuke Horikawa, Safumi Suzuki, and Masahiro Asada. *Wireless data transmission of 30 gbps at*

- a 500-ghz range using resonant-tunneling-diode terahertz oscillator. In *2016 IEEE MTT-S International Microwave Symposium (IMS)*, pages 1–4. IEEE, 2016.
- [54] Chong Han, A Ozan Bicen, and Ian F Akyildiz. *Multi-wideband waveform design for distance-adaptive wireless communications in the terahertz band*. IEEE Transactions on Signal Processing, 64(4):910–922, 2016.
- [55] H-J Song, K Ajito, Y Muramoto, A Wakatsuki, T Nagatsuma, and N Kukutsu. *24 gbit/s data transmission in 300 ghz band for future terahertz communications*. Electronics Letters, 48(15):953–954, 2012.
- [56] SF Busch, M Weidenbach, M Fey, F Schäfer, T Probst, and M Koch. *Optical properties of 3d printable plastics in the thz regime and their application for 3d printed thz optics*. Journal of Infrared, Millimeter, and Terahertz Waves, 35(12):993–997, 2014.
- [57] AD Squires, Evan Constable, and RA Lewis. 3d printing of aspherical terahertz lenses and diffraction gratings. In *Infrared, Millimeter, and Terahertz waves (IRMMW-THz), 2014 39th International Conference on*, pages 1–2. IEEE, 2014.
- [58] Kristian Nielsen, Henrik K Rasmussen, Aurélie J Adam, Paul C Planken, Ole Bang, and Peter U Jepsen. *Bendable, low-loss topas fibers for the terahertz frequency range*. Optics Express, 17(10):8592–8601, 2009.
- [59] Jintao Fan, Yanfeng Li, Minglie Hu, Lu Chai, and Chingyue Wang. *Design of broadband porous-core bandgap terahertz fibers*. IEEE Photonics Technology Letters, 28(10):1096–1099, 2016.
- [60] AI Hernandez-Serrano, M Weidenbach, SF Busch, M Koch, and E Castro-Camus. *Fabrication of gradient-refractive-index lenses for terahertz applications by three-dimensional printing*. JOSA B, 33(5):928–931, 2016.
- [61] Jingbo Liu, Rajind Mendis, and Daniel M Mittleman. *A maxwell’s fish eye lens for the terahertz region*. Applied Physics Letters, 103(3):031104, 2013.
- [62] Daniel Headland, Withawat Withayachumnankul, Michael Webb, Heike Ebendorff-Heidepriem, Andre Luiten, and Derek Abbott. *Analysis of 3d-printed metal for rapid-prototyped reflective terahertz optics*. arXiv preprint arXiv:1605.03246, 2016.

-
- [63] Shashank Pandey, Barun Gupta, and Ajay Nahata. *Terahertz plasmonic waveguides created via 3d printing*. Optics express, 21(21):24422–24430, 2013.
- [64] Dominik Walter Vogt and Rainer Leonhardt. *3d-printed broadband dielectric tube terahertz waveguide with anti-reflection structure*. Journal of Infrared, Millimeter, and Terahertz Waves, 37(11):1086–1095, 2016.
- [65] Dominik Walter Vogt, Jessienta Anthony, and Rainer Leonhardt. *Metallic and 3d-printed dielectric helical terahertz waveguides*. Optics express, 23(26):33359–33369, 2015.
- [66] Casper Larsen, David G Cooke, and Peter Uhd Jepsen. *Finite-difference time-domain analysis of time-resolved terahertz spectroscopy experiments*. JOSA B, 28(5):1308–1316, 2011.
- [67] Dr Eujin Pei, Antonio Lanzotti, Marzio Grasso, Gabriele Staiano, and Massimo Martorelli. *The impact of process parameters on mechanical properties of parts fabricated in pla with an open-source 3-d printer*. Rapid Prototyping Journal, 21(5):604–617, 2015.
- [68] Maik Scheller, Christian Jördens, and Martin Koch. *Terahertz form birefringence*. Optics express, 18(10):10137–10142, 2010.
- [69] Lorenzo Marrucci, C Manzo, and D Paparo. *Optical spin-to-orbital angular momentum conversion in inhomogeneous anisotropic media*. Physical review letters, 96(16):163905, 2006.
- [70] Lorenzo Marrucci, C Manzo, and D Paparo. *Pancharatnam-berry phase optical elements for wave front shaping in the visible domain: Switchable helical mode generation*. Applied Physics Letters, 88(22):221102, 2006.
- [71] Halina Rubinsztein-Dunlop, Andrew Forbes, MV Berry, MR Dennis, David L Andrews, Masud Mansuripur, Cornelia Denz, Christina Alpmann, Peter Banzer, Thomas Bauer, et al. *Roadmap on structured light*. Journal of Optics, 19(1):013001, 2016.
- [72] Lorenzo Marrucci. *The q-plate and its future*. Journal of Nanophotonics, 7(1):078598–078598, 2013.
- [73] Filippo Cardano and Lorenzo Marrucci. *Spin-orbit photonics*. Nature Photonics, 9(12):776–778, 2015.

- [74] AI Hernandez-Serrano, SC Corzo-Garcia, E Garcia-Sanchez, M Alfaro, and E Castro-Camus. *Quality control of leather by terahertz time-domain spectroscopy*. Applied optics, 53(33):7872–7876, 2014.
- [75] Patrick Parkinson, Hannah J Joyce, Qiang Gao, Hark Hoe Tan, Xin Zhang, Jin Zou, Chennupati Jagadish, Laura M Herz, and Michael B Johnston. *Carrier lifetime and mobility enhancement in nearly defect-free core-shell nanowires measured using time-resolved terahertz spectroscopy*. Nano letters, 9(9):3349–3353, 2009.
- [76] John Federici and Lothar Moeller. *Review of terahertz and subterahertz wireless communications*. Journal of Applied Physics, 107(11):6, 2010.
- [77] SF Busch, M Weidenbach, M Fey, F Schäfer, T Probst, and M Koch. *Optical properties of 3d printable plastics in the thz regime and their application for 3d printed thz optics*. Journal of Infrared, Millimeter, and Terahertz Waves, 35(12):993–997, 2014.
- [78] AI Hernandez-Serrano, M Weidenbach, SF Busch, M Koch, and E Castro-Camus. *Fabrication of gradient-refractive-index lenses for terahertz applications by three-dimensional printing*. JOSA B, 33(5):928–931, 2016.
- [79] Alice LS CruzI, Valdir Serrao, Carmem L Barbosa, Marcos AR Franco, Cristiano MB Cordeiro, Alexander Alexander Argyros, and Xiaoli Tang. *3d printed hollow core fiber with negative curvature for terahertz applications*. Journal of Microwaves, Optoelectronics and Electromagnetic Applications (JMoe), 14:45–53, 2015.
- [80] Shashank Pandey, Barun Gupta, and Ajay Nahata. *Terahertz plasmonic waveguides created via 3d printing*. Optics express, 21(21):24422–24430, 2013.
- [81] Zhongqi Zhang, Xuli Wei, Changming Liu, Kejia Wang, Jinsong Liu, and Zhengang Yang. *Rapid fabrication of terahertz lens via three-dimensional printing technology*. Chinese Optics Letters, 13(2):022201–022201, 2015.
- [82] AD Squires, E Constable, and RA Lewis. *3d printed terahertz diffraction gratings and lenses*. Journal of Infrared, Millimeter, and Terahertz Waves, 36(1):72–80, 2015.
- [83] Benedikt Scherger, Maik Scheller, Nico Vieweg, Steven T Cundiff, and Martin Koch. *Paper terahertz wave plates*. Optics express, 19(25):24884–24889, 2011.

- [84] Xuli Wei, Changming Liu, Liting Niu, Zhongqi Zhang, Kejia Wang, Zhengang Yang, and Jinsong Liu. *Generation of arbitrary order besell beams via 3d printed axicons at the terahertz frequency range*. Applied optics, 54(36):10641–10649, 2015.
- [85] Amalya Minasyan, Clément Trovato, Jérôme Degert, Eric Freysz, Etienne Brasselet, and Emmanuel Abraham. *Geometric phase shaping of terahertz vortex beams*. Optics Letters, 42(1):41–44, 2017.
- [86] AI Hernandez-Serrano and E Castro-Camus. *Quasi-wollaston-prism for terahertz frequencies fabricated by 3d printing*. Journal of Infrared, Millimeter, and Terahertz Waves, pages 1–7, 2017.
- [87] Franco Gori. *Polarization basis for vortex beams*. JOSA A, 18(7):1612–1617, 2001.
- [88] Mário FS Ferreira, Enrique Castro-Camus, David J Ottaway, José Miguel López-Higuera, Xian Feng, Wei Jin, Yoonchan Jeong, Nathalie Picqué, Limin Tong, Björn M Reinhard, et al. *Roadmap on optical sensors*. Journal of Optics, 19(8):083001, 2017.
- [89] Stefan F Busch, Jan C Balzer, George Bastian, Graham E Town, and Martin Koch. *Extending the alvarez-lens concept to arbitrary optical devices: Tunable gratings, lenses, and spiral phase plates*. IEEE Transactions on Terahertz Science and Technology, 7(3):320–325, 2017.
- [90] Benedikt Scherger, Maik Scheller, Christian Jansen, Martin Koch, and Karin Wiesauer. *Terahertz lenses made by compression molding of micropowders*. Applied optics, 50(15):2256–2262, 2011.
- [91] Jens Neu, Bernd Krolla, Oliver Paul, Benjamin Reinhard, René Beigang, and Marco Rahm. *Metamaterial-based gradient index lens with strong focusing in the thz frequency range*. Optics express, 18(26):27748–27757, 2010.
- [92] DR Smith, JJ Mock, AF Starr, and D Schurig. *Gradient index metamaterials*. Physical Review E, 71(3):036609, 2005.
- [93] Ruopeng Liu, Qiang Cheng, Jessie Y Chin, Jack J Mock, Tie Jun Cui, and David R Smith. *Broadband gradient index microwave quasi-optical elements based on non-resonant metamaterials*. Optics express, 17(23):21030–21041, 2009.

-
- [94] Oliver Paul, Benjamin Reinhard, Bernd Krolla, René Beigang, and Marco Rahm. *Gradient index metamaterial based on slot elements*. Applied Physics Letters, 96(24):241110, 2010.
- [95] Rajind Mendis, Masaya Nagai, Yiqiu Wang, Nicholas Karl, and Daniel M Mittleman. *Terahertz artificial dielectric lens*. Scientific reports, 6, 2016.
- [96] Winston E Kock. *Metallic delay lenses*. Bell Labs Technical Journal, 27(1):58–82, 1948.
- [97] Winston E Kock. *Metal-lens antennas*. Proceedings of the IRE, 34(11):828–836, 1946.
- [98] John Brown. *Artificial dielectrics having refractive indices less than unity*. Proceedings of the IEE-Part IV: Institution Monographs, 100(5):51–62, 1953.
- [99] Víctor Torres, Víctor Pacheco-Peña, Pablo Rodríguez-Ulibarri, Miguel Navarro-Cía, Miguel Beruete, Mario Sorolla, and Nader Engheta. *Terahertz epsilon-near-zero graded-index lens*. Optics express, 21(7):9156–9166, 2013.
- [100] Rajind Mendis and Daniel M Mittleman. *Comparison of the lowest-order transverse-electric (te 1) and transverse-magnetic (tem) modes of the parallel-plate waveguide for terahertz pulse applications*. Optics express, 17(17):14839–14850, 2009.
- [101] Rajind Mendis, Jingbo Liu, and Daniel M Mittleman. *Terahertz mirage: Deflecting terahertz beams in an inhomogeneous artificial dielectric based on a parallel-plate waveguide*. Applied Physics Letters, 101(11):111108, 2012.
- [102] Constantine A Balanis. *Advanced engineering electromagnetics*. John Wiley & Sons, 1999.
- [103] David George Voelz. *Computational fourier optics: a MATLAB tutorial*. SPIE press Bellingham, WA, 2011.
- [104] Allen Taflove and Susan C Hagness. *Computational electrodynamics: the finite-difference time-domain method*. Artech house, 2005.